

# In-depth investigation of thermochemical performance in a heat battery: Cyclic analysis of $K_2CO_3$ , $MgCl_2$ and $Na_2S$



L.C. Sögütöglu<sup>a</sup>, P.A.J. Donkers<sup>b</sup>, H.R. Fischer<sup>b</sup>, H.P. Huinink<sup>a,\*</sup>, O.C.G. Adan<sup>a,b</sup>

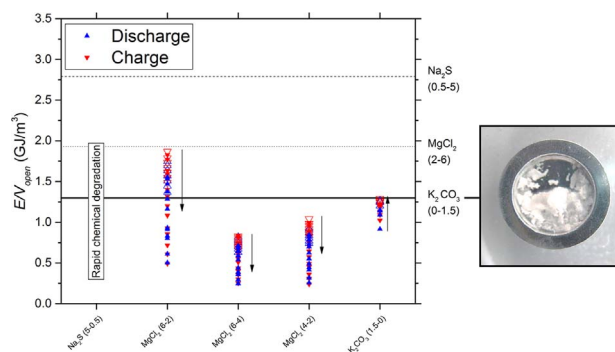
<sup>a</sup> Technical University Eindhoven, Den Dolech 2, 5600 MB Eindhoven, The Netherlands

<sup>b</sup> TNO, De Rondom 1, 5612 AP Eindhoven, The Netherlands

## HIGHLIGHTS

- $K_2CO_3$  is a promising salt for thermochemical heat battery application.
- $1\text{ m}^3$  of  $K_2CO_3$  can store 15–66 GJ annually, repeated over at least 20 years.
- $CO_2$  adsorption accompanies hydration of  $K_2CO_3$ , without effecting thermochemical performance.
- $Na_2S$  and  $MgCl_2$  are salts with a higher storage density than  $K_2CO_3$ .
- $Na_2S$  and  $MgCl_2$  face chemical degradation in thermochemical heat battery application.

## GRAPHICAL ABSTRACT



## ARTICLE INFO

### Keywords:

Thermo chemical heat storage  
Salt hydrates  
Phase diagram  
Chemical stability  
Side reactions  
Enthalpy of hydration  
Energy density

## ABSTRACT

Thermochemical materials  $K_2CO_3$ ,  $MgCl_2$  and  $Na_2S$  have been investigated in depth on energy density, power output and chemical stability in view of domestic heat storage application, presenting a critical assessment of potential chemical side reactions in an open and closed reactor concept. These materials were selected based on a recent review on all possible salt hydrates, within the frame of a thermochemical heat battery and considering recent advances in heat storage application. Judged by gravimetric and calorimetric experiments in operating conditions and worst-case-scenario conditions,  $K_2CO_3$  is recommended for both an open and closed system heat battery. The compound is chemically robust with a material level energy density of  $1.28\text{ GJ/m}^3$  in an open system and  $0.95\text{ GJ/m}^3$  in a closed system, yielding a power output of  $283\text{--}675\text{ kW/m}^3$ .  $Na_2S$  and  $MgCl_2$  on the other hand are chemically not robust in heat storage application, although having a higher energy density, output power and temperature in one cycle.

## 1. Introduction

Society's progressive shift from carbon-based to renewable energy has led to new areas in energy research. The first global conference on energy storage in Paris, 2014 concluded that harvesting, conversion and storage of solar energy is essential to achieve the European goal of an energy-neutral built environment in 2050. The building sector

accounts for the largest share of energy consumption (37% Europe wide). As two third of the built environment in 2050 is made up of currently existing buildings, the solution should be realised with the current building stock [1]. Because a significant part (around 70%) of the energy consumption in the European residential sector is related to domestic space heating and hot tap water [2,3] a heat battery technique in view of domestic heat consumption is highly desired.

\* Corresponding author.

E-mail address: [h.p.huinink@tue.nl](mailto:h.p.huinink@tue.nl) (H.P. Huinink).

<https://doi.org/10.1016/j.apenergy.2018.01.083>

Received 22 August 2017; Received in revised form 22 January 2018; Accepted 27 January 2018

Available online 20 February 2018

0306-2619/© 2018 The Author(s). Published by Elsevier Ltd. This is an open access article under the CC BY license

(<http://creativecommons.org/licenses/by/4.0/>).

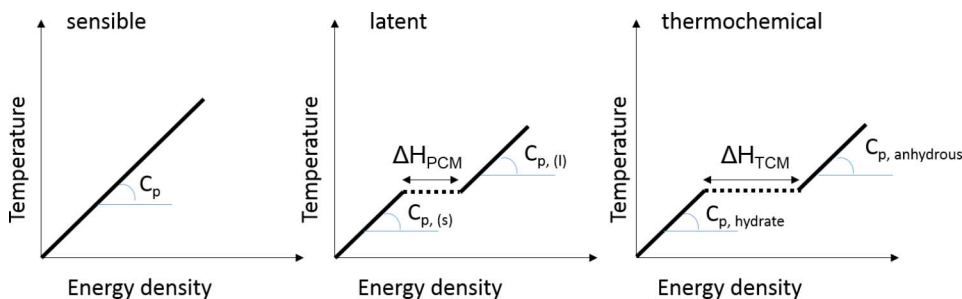


Fig. 1. Schematic diagram of temperature against energy density for sensible, latent and thermochemical heat storage. Sensible heat storage is based on increasing the temperature of a high heat capacity storage material, and hereby storing the heat. Latent heat storage can store a larger amount of heat in a much shorter temperature range, thanks to the phase change. Thermochemical heat storage can store the largest amount of heat, in heatloss-free way by means of chemisorption or physisorption of a sorbent gas.

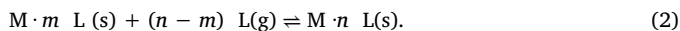
Given the societal urge for heat storage, the number of reviews on sensible, latent and thermochemical energy storage materials has increased in the past decades, funnelling towards application progressively [4–8].

Heat storage in materials is possible in three ways, shown schematically in Fig. 1. Sensible heat storage is the simplest way to store heat and is based on increasing the temperature of a high heat capacity storage material, hereby storing the heat.

Latent heat storage is based on the released latent heat during a phase transition. A phase change material (PCM) can store a larger amount of heat in a much shorter temperature range [9], thanks to the phase transition:

$$M(s) \rightleftharpoons M(l). \tag{1}$$

A thermochemical reaction on the other hand, can store an even larger amount of heat in heat loss-free way, by means of chemisorption or physisorption of a sorbent gas. As such, high energy density and heat-loss free storage are intrinsic material properties of thermochemical materials (TCM), noticed already in 1958 by Goldstein [10], who was the first to suggest the concept of a thermochemical heat battery. The heat is released when the sorbent gas adsorbs to the storage material [6], reaction (2):



An essential difference between a phase change and a thermochemical reaction is that a phase change depends on temperature only, whereas a thermochemical reaction has an extra control parameter: namely the pressure of the sorbent (gas), illustrated schematically in the phase diagram in Fig. 2.

In a recent review on advances in thermal energy storage, Lizana

et al. [4] conclude that the highest potential for competitive energy efficiency lies in latent and sensible energy storage systems presenting a volumetric thermal energy storage density up to 430 and 250 MJ/m<sup>3</sup> respectively. Application of PCMs in free-cooling ventilation systems and solar energy storage solutions for short and long-term storage periods are highlighted as promising. Their analysis shows that currently, no material for thermochemical energy storage is available that satisfies all the requirements for energy storage solutions for short and long-term storage periods, despite the potentially high energy density achievable (up to 1510 MJ/m<sup>3</sup>) and long term storage ability of TCMs. The authors analyse that additional research efforts must be pursued to optimise operation conditions, storage cycle efficiency, material cost and system design.

Contemporary with Lizana, Donkers [5] had published a review on thermochemical materials, considering operating conditions, volume change, availability, cost and environmental impact in methodological way based on thermodynamic data of 563 thermochemical reactions in total in search for the most promising thermochemical material in view of a technology break-through. Donkers et al. suggested K<sub>2</sub>CO<sub>3</sub> for use in domestic application with a volumetric storage density of 1300 MJ/m<sup>3</sup>. In line with the review of Lizana, Donkers categorised MgSO<sub>4</sub> and CaCl<sub>2</sub> unsuitable for low temperature domestic heat storage judged by temperature lift. Furthermore, Na<sub>2</sub>S and MgCl<sub>2</sub> were noted as TCMs with a higher energy density than K<sub>2</sub>CO<sub>3</sub>, supporting choices of present research programs [13,14].

Latent heat storage has promising competitive energy efficiency for passive applications like temperature mitigation [15], it is not suitable for thermal energy storage in the form of a heat battery. The low storage density and the difficulty to control the phase change are current barriers to technology break-through in view of longer term storage. Water-based sensible heat storage on the other hand is certainly uncompetitive on material level, considering the average price of 1.20 €/m<sup>3</sup>. However, the main bottleneck of sensible heat storage modules in 2020 indicate 300–900 €/m<sup>3</sup> on reactor level [16], mainly due to high isolation costs for the sensible technique.

In recent heat battery projects like MERITS (2007–2013) and E-HUB (2010–2014) thermochemical materials Na<sub>2</sub>S and MgCl<sub>2</sub> were used, with an average cost of 180 and 650 €/m<sup>3</sup> respectively on material level [5,13,14]. Although MgCl<sub>2</sub> was found promising for domestic space heating and hot tap water purposes, later studies of MgCl<sub>2</sub> showed that the compound might be less alluring than initially thought, due to chemical degradation with HCl formation inside the reactor [17]. For Na<sub>2</sub>S on the other hand, no calorimetric verification of the effective heat output has been reported so far.

It was not until recently that the high impact of chemical stability was recognised on the level of thermochemical reactor design (open or a closed system), discharge periods (days-months) and energy density, as critical reviews and first reactor trials have started just recently. Recent insights request that heat battery targets should be evaluated given the chemical characteristic of the thermochemical material of use.

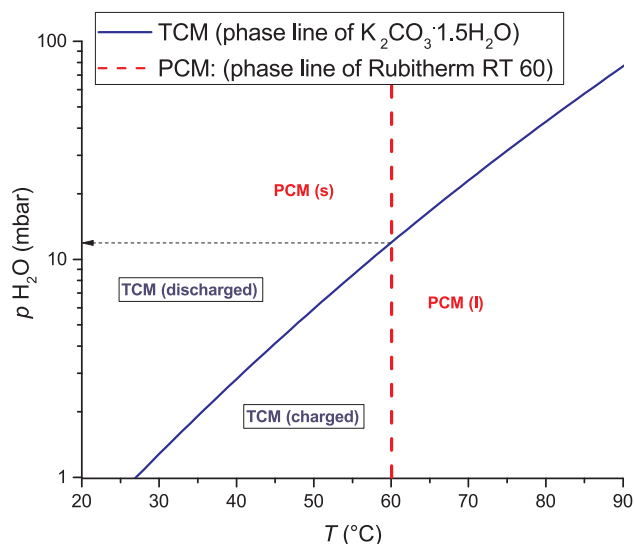


Fig. 2. Schematic phase diagrams of a PCM (K<sub>2</sub>CO<sub>3</sub>) [11] and a TCM (Rubitherm RT60) [12]. The PCM has a phase transition at 60 °C, regardless of external vapour pressure. The TCM has a phase change at 60 °C when the external vapour pressure is 12 mbar.

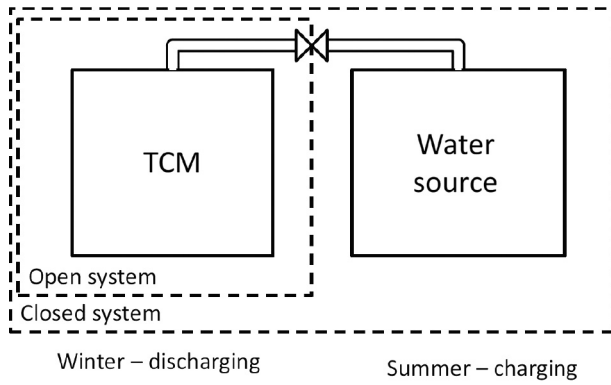


Fig. 3. Schematic representation of the seasonal TCM-module concept, adapted from Donkers et al. [5]. The TCM compartment is connected to a water source through a valve, which can be operated according to the need of energy supply. The water source acts as an evaporator during discharging the TCM in winter (typical temperatures of 10 °C, corresponding to 12 mbar) and as a condenser during charging in summer (typical temperatures of 17 °C, corresponding to 20 mbar). In a closed system, both water source and TCM-compartment are integrated inside the module, and the complete module operates in vacuum. In an open system, the water source is outside the module and the TCM is in contact with ambient air.

In the current Horizon 2020 program, the European Union targets an energy density of 1.5 GJ/m<sup>3</sup> and 420 kWh/m<sup>3</sup>, with performance over 20 years delivering 5 kW for a single family home [1].

In this work, we present the first in-depth study of the thermochemical performance of highly relevant heat storage materials K<sub>2</sub>CO<sub>3</sub>, MgCl<sub>2</sub> and Na<sub>2</sub>S, putting the chemical stability of the thermochemical materials to the test in an open and closed reactor environment. Calorimetric heat in- and output has been studied in depth in cyclic way for the first time, concluding with a material recommendation for thermochemical heat storage application in the built environment.

## 2. Heat storage

### 2.1. Definition of system and energy density

Two types of thermochemical reactor concepts are distinguished: open and closed systems, presented schematically in Fig. 3 [5]. The reactor operates in West-European conditions, with a typical water vapour pressure of 12 mbar. This pressure is often used as guideline in present heat storage research projects [13,18], but can be lower or higher, depending on the exact temperature of the water source.

The water source has a temperature of approximately 10 °C in winter, corresponding to an equilibrium pressure of 12 mbar. In a simplistic view, the TCM compartment is connected to a water source through a valve, which can be operated according to the need of energy supply. The water source acts as a humidifier with a constant vapour pressure of 12 mbar during discharging in winter and as a condenser during charging in summer at typical water temperatures of 17 °C (corresponding to a constant vapour pressure 20 mbar).

An open system is in open connection with the atmosphere, which makes chemical degradation due to reactive gasses other than H<sub>2</sub>O possible. The water source of the open system is not a part of the reactor. The energy density of an open system for the generic thermochemical reaction (2) is given as:

$$(E/V)_{open} = \frac{E}{V_n}$$

$$(E/V)_{open} = \frac{(n-m) \cdot \Delta H_{m \rightarrow n}^0}{\frac{M_n}{\rho_n}} \quad (3)$$

in which  $\Delta H_{m \rightarrow n}^0$  is the reaction enthalpy [J/mol],  $M_n$  [kg/mol] is the molar mass of the highest hydrate and  $\rho_n$  [kg/m<sup>3</sup>] is the crystal density of the highest hydrate.

A closed system operates in vacuum, in the absence of any reactive

gasses other than water. For a closed system, the water source is a part of the reactor and the volume of water molecules involved in the reaction is considered as well in calculation of the energy density:

$$(E/V)_{closed} = \frac{E}{V_n + V_W}$$

$$(E/V)_{closed} = \frac{(n-m) \cdot \Delta H_{m \rightarrow n}^0}{\frac{M_n}{\rho_n} + (n-m) \cdot \frac{M_W}{\rho_W}}$$

$$(E/V)_{closed} = (E/V_{open}) \cdot \frac{1}{1 + (n-m) \cdot \frac{\rho_n \cdot M_W}{M_n \cdot \rho_W}} \quad (4)$$

with  $M_W$  [kg/mol] the molar mass of water and  $\rho_W$  [kg/m<sup>3</sup>] the density of water. In other words, a closed system has a smaller energy density than an open system, because of the water source housed inside the system.

### 2.2. Thermodynamic properties of the TCM

The output temperature of a TCM depends on its pressure-temperature phase diagram. Therefore, phase diagrams of thermochemical reactions were constructed following Donkers et al., fitting experimental p,T-data reported in literature [18–20] with the basic thermodynamic Eq. (5). Eq. (5) describes the equilibrium between the solid phase and the vapour phase (as given in reaction (2)), and holds for any pure substance, under conditions of low pressure [5,21]:

$$-\ln \frac{p}{p^0} = \frac{\Delta G_r^0}{RT} = \frac{\Delta H_r^0}{R} \cdot \frac{1}{T} - \frac{\Delta S_r^0}{R} \quad (5)$$

with  $R$  the gas constant,  $R = 8.31451$  J/K/mol,  $T$  [K] the temperature,  $p$  [bar] the vapour pressure, and  $p^0$  the reference pressure. The molar enthalpy  $\Delta H_r^0$  [J/mol] and entropy  $\Delta S_r^0$  [J/mol/K] of hydration are used as linear fitting parameters.

The phase diagram of K<sub>2</sub>CO<sub>3</sub> is shown as an example in Fig. 4. The fit allows to calculate the theoretical energy density of the TCM via the hydration enthalpy and parametrises the output temperature at the typical vapour pressure of 12 mbar in winter. A water vapour pressure of 12 mbar (solid arrows in Fig. 4) corresponds to an equilibrium TCM temperature of 59 °C. This means that K<sub>2</sub>CO<sub>3</sub> can heat up to 59 °C upon hydration when exposed to a water source of 12 mbar (10 °C) in winter. The pressure difference  $\Delta P$  between TCM and water source will drive the hydration, i.e., until 59 °C is reached. On the other hand, heating the TCM to 65 °C (dashed arrows) produces a vapour pressure of 20 mbar.

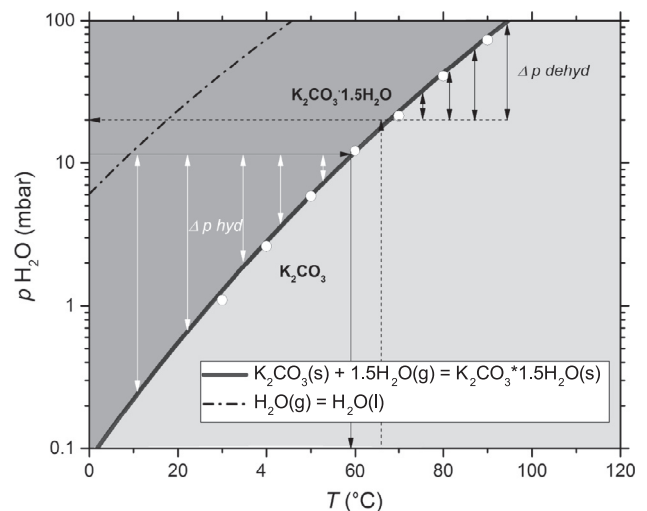


Fig. 4. Phase diagram of K<sub>2</sub>CO<sub>3</sub> showing the thermochemical reaction (solid line) [19]. Liquid – gas equilibrium of water is indicated by the dash-dotted line. A water vapour pressure of 12 mbar corresponds to a TCM temperature of 59 °C (solid arrow). The pressure difference  $\Delta P$  between K<sub>2</sub>CO<sub>3</sub> and the water source drives the hydration. Measured pressures are represented by dots.

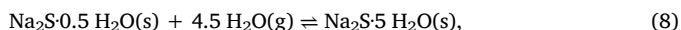
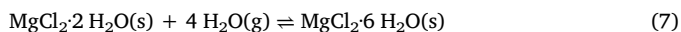
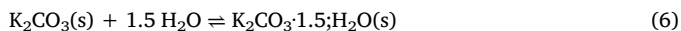
**Table 1**

Thermodynamic criteria for selecting hydrates suitable for heat storage considering domestic application.  $E/V$  in this table is the energy density of the TCM, in which only the volume of the TCM is considered. A vapour pressure of 12 and 20 mbar corresponds to a water temperature of 10 and 17 °C in the reservoir respectively.

Filter criteria	Cut-off value
$E/V$ [GJ/m <sup>3</sup> ]	> 1.3
Hydration	
$p$ [mbar]	12
$T$ [°C]	> 50
Dehydration	
$p$ [mbar]	20
$T$ [°C]	< 120
$T_{melting}$	> $T_{dehydration}$

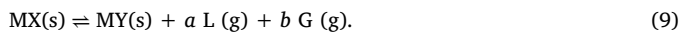
This means that dehydration of the TCM is possible when exposed to a water source of maximum 17 °C (20 mbar) in summer.

The thermodynamic selection criteria as applied by Donkers et al. are summarised in Table 1. Thermochemical reactions (6)–(8) were selected for a comprehensive performance study after careful analysis of operating pressure, costs and present research projects [5,13,14]. Table 2 lists the selected salts and their thermodynamic properties. The deliquescence point of salts is mentioned explicitly, because deliquescence (or liquefaction in general) should be avoided to maintain shape and thermal stability.



### 2.3. Stability after cycling

A critical review on the chemical stability of  $\text{K}_2\text{CO}_3$ ,  $\text{Na}_2\text{S}$  and  $\text{MgCl}_2$  was performed by identifying potential side reactions and constructing phase diagrams as in the case of the thermochemical reaction. Reaction (9) is an example involving sorbent gas L (representing water) and foreign gas G in the degradation of salt MX to thermochemically inactive product MY:



Phase lines are constructed by solving the corresponding thermodynamic Eq. (10) for phase equilibrium in terms of  $p_L$  [22,21]:

$$\ln \left[ \left( \frac{p_L}{p^0} \right)^a \cdot \left( \frac{p_G}{p^0} \right)^b \right] = \frac{\Delta G_r^0}{RT} = \frac{\Delta H_r^0}{R} \cdot \frac{1}{T} - \frac{\Delta S_r^0}{R}, \quad (10)$$

in which  $p_L$  and  $p_G$  are the partial vapour pressure of water and the foreign gas [bar] respectively, and  $p^0$  is the standard pressure.  $p_G$  is chosen at typical values expected in atmospheric conditions. The enthalpy and entropy of reaction,  $\Delta H_r^0$  and  $\Delta S_r^0$ , are calculated from tabulated values [11] and normalised to one mole of gaseous sorbent L (representing  $\text{H}_2\text{O}$ ):

**Table 2**

List of investigated thermochemical reactions. These reactions have a suitable temperature output at ambient water vapour pressures in typical North-West European dwellings. Filter criteria as stated by Donkers et al. are listed in Table 1. The salts are sorted descending based on the theoretical energy density of an open system.

Salt	Transition	Energy density open system (GJ/m <sup>3</sup> )	Energy density closed system (GJ/m <sup>3</sup> )	$T$ discharge at 12 mbar (°C)	$T$ charge at 20 mbar (°C)	Deliquescence vapour pressure at 25 °C (mbar)
$\text{Na}_2\text{S}$ [18]	0.5-5	2.79	1.58	66	82	> 11
$\text{MgCl}_2$ [20]	2-4-6	1.93	1.24	61	104	10
$\text{K}_2\text{CO}_3$ [11]	0-1.5	1.3	0.96	59	65	14

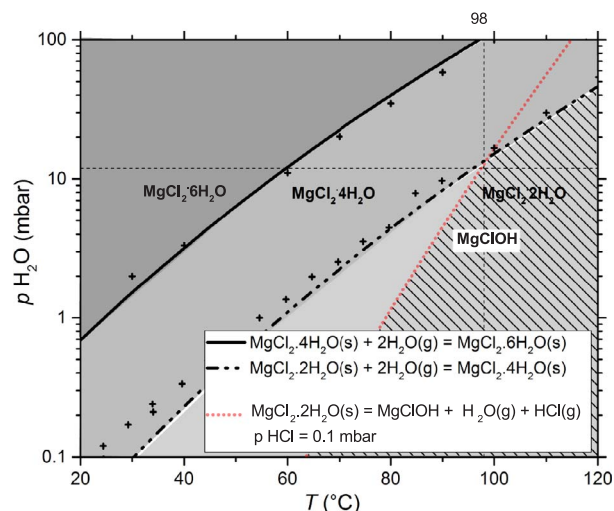
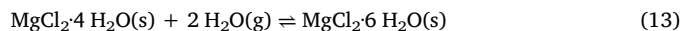
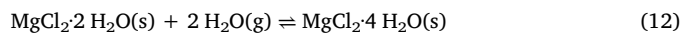
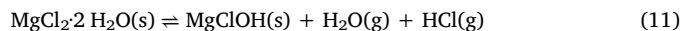


Fig. 5. Phase diagram of  $\text{MgCl}_2$  showing calculated phase boundaries of hydration and chemical degradation (in legend) based on energies of formation [11]. Chemical degradation is expected in the hatched area at  $p_{\text{HCl}} = 0.1$  mbar. The vertical dotted line at 98 °C denotes the minimum temperature at which HCl formation starts at typical working conditions of 12 mbar. Crosses represent experimental pressures and temperatures as reported in literature. Area of the dihydrate phase is featured light grey, higher hydrate phases are shown as darker grey.

$$\Delta H_r^0 = \left( \sum_{\text{products}} H_i^0 - \sum_{\text{reactants}} H_i^0 \right) / a$$

$$\Delta S_r^0 = \left( \sum_{\text{products}} S_i^0 - \sum_{\text{reactants}} S_i^0 \right) / a$$

In this way, the phase diagram of the side reaction can be superimposed with the thermochemical reaction, as a function of water vapour pressure. As an example, Fig. 5 shows a calculated phase diagram of  $\text{MgCl}_2$  in the following reactions, with HCl as foreign gas G:



The dotted line denotes the degradation of  $\text{MgCl}_2 \cdot 2 \text{H}_2\text{O}$  at  $p_{\text{HCl}} = 0.1$  mbar. Superimposing phase lines of hydration and degradation allows to mark the pressure-temperature area in which the side product  $\text{MgClOH}$  is thermodynamically stable; hatched in Fig. 5. In other words, reaction (11) is expected in the hatched area. Analogously, reaction (12) is expected in the medium grey area and reaction (13) is expected in the dark grey area.

## 3. Materials and methods

### 3.1. Sample preparation

$\text{K}_2\text{CO}_3 \cdot 1.5 \text{H}_2\text{O}$  (sieved to 50–164  $\mu\text{m}$ ) and  $\text{MgCl}_2 \cdot 6 \text{H}_2\text{O}$  (sieved to 500–1000  $\mu\text{m}$ ) were purchased from Sigma-Aldrich (pro analysis) and

were stored inside a desiccator above a saturated solution of  $\text{CH}_3\text{COOK}$  (22% RH at 21 °C) without any further purification. Samples were kept at 22% RH to prevent overhydration or deliquescence.  $\text{Na}_2\text{S}\cdot 9\text{H}_2\text{O}$  was purchased from Acros (pro analysis) and was recrystallised to polycrystalline  $\text{Na}_2\text{S}\cdot 5\text{H}_2\text{O}$  (estimated size 50–164  $\mu\text{m}$ ).

A second set of experiments was conducted on 0.5–1 mm grains.  $\text{K}_2\text{CO}_3\cdot 1.5\text{H}_2\text{O}$  and  $\text{MgCl}_2\cdot 6\text{H}_2\text{O}$  (Sigma-Aldrich, pro analysis) were sieved to 0.5–1 mm grains. Recrystallised  $\text{Na}_2\text{S}\cdot 5\text{H}_2\text{O}$  (Acros, pro analysis) was submerged in liquid  $\text{N}_2$  and 0.5–1 mm grains were selected in liquid  $\text{N}_2$  conditions to prevent possible chemical degradation during sample preparation. Samples were stored in air tight vials to prevent overhydration or chemical degradation [23–26].

### 3.1.1. $\text{Na}_2\text{S}$ recrystallisation

A glass container was placed in an oil bath with stirrer. The flask was connected with a  $\text{N}_2$ /vacuum inlet with an over pressure safety valve. A commercial  $\text{H}_2\text{S}$  sensor was placed in the vicinity of the flask, because of the possibility of  $\text{H}_2\text{S}$  formation. The flask was filled with 500 g  $\text{Na}_2\text{S}\cdot 9\text{H}_2\text{O}$  and closed with an overpressure valve. 250 g of demi water was added. The flask was heated until 115 °C. After 60 min a slurry of  $\text{Na}_2\text{S}$  was obtained and another 100 g demi water was added. The solution was heated further until 125 °C and stirred for another 60 min. The salt was completely dissolved and a homogeneous yellow solution was formed. The solution was subsequently cooled to 60 °C to allow the crystallisation of  $\text{Na}_2\text{S}\cdot 5\text{H}_2\text{O}$ . White crystals were filtered off with a heated filter at 60 °C. The yield was 464 g.

A second recrystallisation was performed on the obtained precipitant to further enhance the purity of  $\text{Na}_2\text{S}\cdot 5\text{H}_2\text{O}$ . The glass container was filled with 464 g  $\text{Na}_2\text{S}\cdot 5\text{H}_2\text{O}$  crystals. 50 g demi water was added. The mixture was heated for 1 h at 125 °C to ensure complete dissolution of the salt and crystallization of  $\text{Na}_2\text{S}\cdot 5\text{H}_2\text{O}$  was induced by cooling the mixture to 60 °C, while stirring at low rotational speeds. The crystals were filtered off with a heated filter at 60 °C. The yield of  $\text{Na}_2\text{S}\cdot 5\text{H}_2\text{O}$  crystals was 115 g. The obtained product was wet and was therefore placed in a vacuum oven to remove excess of water.  $\text{Na}_2\text{S}\cdot 5\text{H}_2\text{O}$  was kept in air-tight vials after recrystallisation to avoid degradation and  $\text{H}_2\text{S}$ -formation in air [23,24].

### 3.2. Infrared spectroscopy

Infrared absorbance of samples is measured using a Shimadzu FTIR 8400S with a horizontal ATR (attenuated total reflectance) crystal. Before analysis, the crystal surface is cleaned with a tissue soaked in water and a tissue soaked in isopropanol and left to dry. The sample is applied in powdered form on the surface of the crystal and pressed during the measurement using a screw for optimum signal/noise ratio. The spectrum is collected by co-adding 48 scans at a resolution of 4.0  $\text{cm}^{-1}$  and automatic gain.

### 3.3. Pressure-Temperature ( $p,T$ ) measurements

The experimental setup to measure equilibrium  $pT$  lines is shown schematically in Fig. 6. The pressure - temperature setup consists of a stainless steel sample chamber which is connected to an Arduino® absolute pressure sensor and via a valve to a vacuum pump. Tubing consists of 6 mm outside diameter stainless steel and connections are made with Swagelok® fittings. The sample chamber which needs frequent assembly and disassembly is connected via a KF flange with a rubber o-ring and mated by a circumferential clamp. The sample chamber is heated with an electric band heater and the temperature is controlled with an Eurotherm® 2216e controller. The complete setup is heated with an electric heating wire and all parts are insulated to avoid internal condensation. For measuring the equilibrium phase line, the hydrated salt is positioned inside the sample chamber. The sample chamber is heated and the temperature is kept constant until an equilibrium pressure is reached. The temperature is increased stepwise and

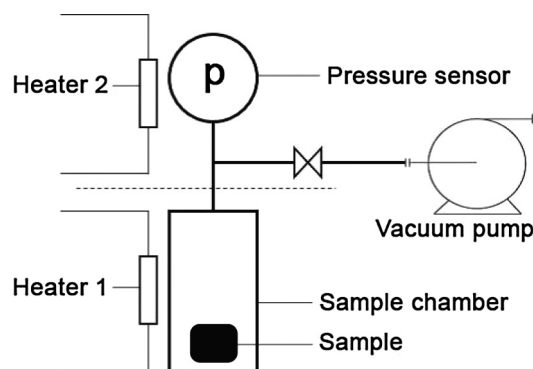


Fig. 6. Schematic representation of the pressure temperature measurement setup, used to measure phase lines of salt hydrates. The system is thermally isolated. Sample and surrounding are brought to the same temperature simultaneously using heater 1 and 2 respectively. After equilibration, the water vapour pressure is measured using a pressure sensor.

the next equilibrium pressure is determined. From these data points the  $pT$  line can be constructed.

### 3.4. Thermal analysis

A thermogravimetric analyser of type Mettler-Toledo TGA/SDTA 851e was equipped with a homebuilt humidity generator. The purge gas ( $\text{N}_2$  or air, flow rate 300 mL/min) was brought to the desired water vapour pressure by mixing dry gas (0% RH) and wet gas (100% RH) at a controlled temperature of 21 °C. The water vapour pressure was calibrated with an accuracy of  $\pm 1$  mbar using the gravimetric signal at the deliquescence point of  $\text{LiCl}$ ,  $\text{CH}_3\text{COOK}$ ,  $\text{K}_2\text{CO}_3$ ,  $\text{MgCl}_2$  and  $\text{MgNO}_3$  at 25 °C and  $\text{LiCl}$  at 40, 50, 55 and 60 °C [26]. Actual sample temperatures were recorded at the bottom of the pan and temperature calibration was performed using the Simultaneous Differential Thermal Analysis (SDTA)-signal of melting points of Indium, Zinc and Aluminium. In case of an endothermic process such as melting, a differential signal is observed [27]. Buoyancy causes a deviation of 2% sample mass between maximum and minimum temperature, which is negligible in the multi-cyclic experiments.

A differential scanning calorimeter of type Mettler-Toledo DSC25 was equipped with a homebuilt humidity generator. The purge gas ( $\text{N}_2$  or air, flow rate 300 mL/min) was brought to the desired water vapour pressure by mixing dry gas (0% RH) and wet gas (100% RH) at a controlled temperature of 21 °C. The humidified purge gas is brought to furnace temperature using a purge gas heat exchanger before reaching the sample. This enables that at any temperature and partial water vapour pressure, the DSC provides a heat flow due to the temperature difference  $\Delta T$  between sample and reference pan only. The water vapour pressure was calibrated with an accuracy of  $\pm 1$  mbar using the exothermic DSC-signal at the deliquescence point of  $\text{CH}_3\text{COOK}$ ,  $\text{K}_2\text{CO}_3$  and  $\text{MgCl}_2$  at 25 °C [26]. Temperature calibration was performed using melting points of  $\text{Na}_2\text{SO}_4\cdot 10\text{H}_2\text{O}$ , Indium and Zinc with an accuracy of  $\pm 0.3$  °C [28]. Heat flow was calibrated with an accuracy of  $\pm 5\%$  using the melting enthalpy of Indium and Zinc [28,29].

40  $\mu\text{L}$  Mettler-Toledo standard aluminium pans without lid were used in TGA and DSC experiments. Aluminium is suitable as sample holder for multi-cyclic experiments. It has a high thermal conductivity and is not corroded by the salt when exposed to water vapour.

Dehydration/rehydration was performed in cyclic way by heating and cooling the sample with rates of 0.5 K/min at  $p_{\text{H}_2\text{O}} = 7.5$  mbar and 10 K/min at  $p_{\text{H}_2\text{O}} = 12$  mbar.

Sample masses are correlated to the water loading (mol water/mol salt) via Eq. (14):

$$\text{Loading} = x - \frac{m_x - m(t)}{M_w} \cdot \frac{M_x}{m_x} \quad (14)$$

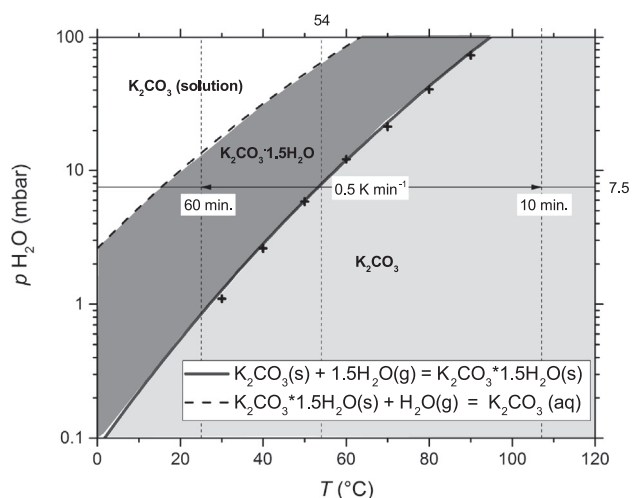


**Fig. 7.** Phase diagram of  $K_2CO_3$  [19]. Experimental conditions are indicated schematically. Temperature range 25–107 °C,  $p_{H_2O} = 7.5$  mbar, heating/cooling rate 0.5 K/min. The p,T-line was validated experimentally, because of limited p,T data in literature; crosses represent own measurements. Area of the anhydrous phase is featured light grey, the hydrate phase is shown as darker grey. The thermodynamic onset temperature of the 0–1.5 transition at  $p_{H_2O} = 7.5$  mbar is indicated at 54 °C. The deliquescence transition [26] is shown by the dashed line.

where  $M_x$  and  $M_w$  (g/mol) are the molar masses of the x-hydrate and water and  $m(t)$  and  $m_x$  (g) are the actual and x-hydrate masses of the sample.  $x = 6, 5$  and  $1.5$  for  $MgCl_2 \cdot xH_2O$ ,  $Na_2SxH_2O$  and  $K_2CO_3 \cdot xH_2O$  respectively at  $p_{H_2O} = 7.5$  mbar and  $T = 35$  °C, based on phase diagrams.

## 4. Results and discussion

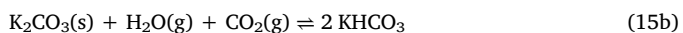
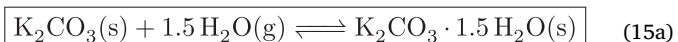
### 4.1. $K_2CO_3$ 0–1.5 transition

Present literature suggests that  $H_2O$  uptake by  $K_2CO_3$  to form  $K_2CO_3 \cdot 1.5H_2O$  releases 65.8 kJ/mol water, corresponding to a maximum energy density of 1.30 GJ/m<sup>3</sup> [19,5]. The thermochemical reaction is given in reaction (15a) and the corresponding phase diagram is presented in Fig. 7 [19].

After additional literature study on  $K_2CO_3$  reactivity [11,25,30–33] reactions (15b) and (15c) were found possible to occur in conditions used for thermochemical heat storage. Phase diagrams of reactions (15a)–(15c) are superimposed in Fig. 8 [11] to identify thermodynamic conditions for chemical degradation. The hatched area represents the conditions in which  $KHCO_3$  formation occurs. In other words, in this area  $CO_2$  is adsorbed by  $K_2CO_3$  or  $K_2CO_3 \cdot 1.5H_2O$ .

Because  $KHCO_3$  formation involves  $CO_2$ , degradation is expected to occur in an open system. Open and closed system reactive conditions were mimicked in experiments by using air and  $N_2$  as purge gas respectively.

Experimental conditions at which the multi-cyclic energy density was studied are schematically included in the phase diagram in Fig. 7.  $K_2CO_3$  was hydrated and dehydrated at  $p_{H_2O} = 7.5$  mbar inside TGA by adapting the sample temperature between 25 °C and 107 °C with a rate of 0.5 K/min. An isothermal conditioning period of 60 min at 25 °C and 10 min at 107 °C was used to complete the (de)hydration before starting the next cycle.



Prior to thermal analysis,  $K_2CO_3 \cdot 1.5H_2O$  (50–164  $\mu$ m) was stored in

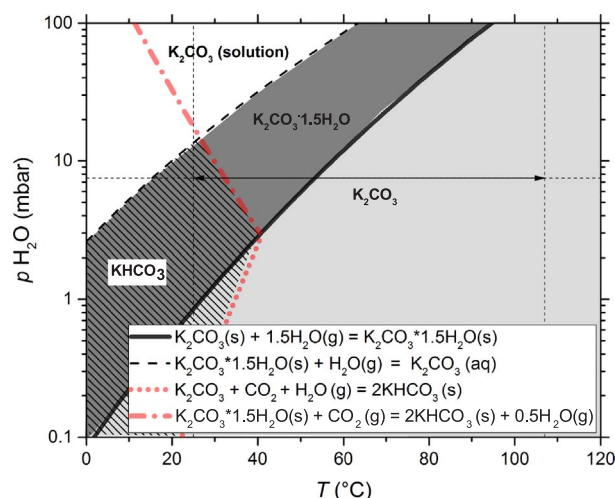


**Fig. 8.** Phase diagram for reactions (15a)–(15c) at  $p_{CO_2} = 0.4$  mbar (i.e. atmospheric conditions) [11]. The theoretical p,T-line [19] is based on extrapolation of not recent p,T-measurements and is therefore validated experimentally (open circles). The deliquescence transition [26] (dashed line) is added for completeness. Experimental working temperatures (hydration at 25 °C and dehydration at 107 °C) and pressure ( $p_{H_2O} = 7.5$  mbar) are indicated by dotted lines.  $KHCO_3$  formation occurs in the grey area.

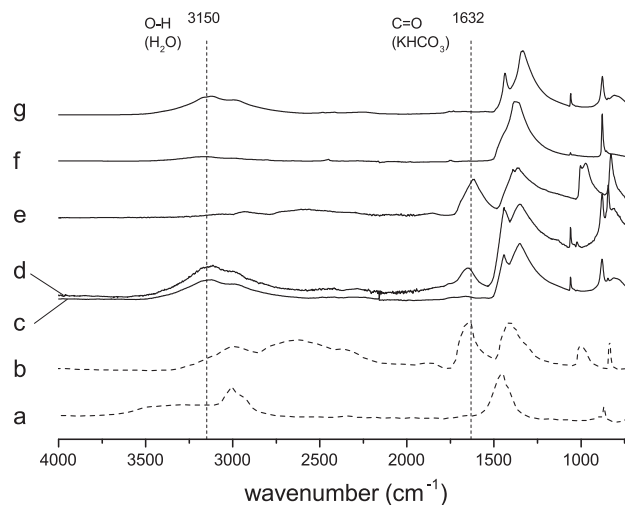


**Fig. 9.** IR spectra of  $KHCO_3$ ,  $K_2CO_3$  and  $K_2CO_3 \cdot 1.5H_2O$ . Experimental and literature spectra are shown in solid and dotted lines respectively [34]. (a)  $K_2CO_3$ , (b)  $KHCO_3$ , (c)  $K_2CO_3 \cdot 1.5H_2O$  pro analysis Sigma-Aldrich, (d)  $K_2CO_3 \cdot 1.5H_2O$  pro analysis Sigma-Aldrich after 8 weeks of storage in air at 25 °C, (e)  $KHCO_3$  pro analysis Sigma-Aldrich, (f)  $K_2CO_3$  after dehydration at 130 °C and (g)  $K_2CO_3$  after 1 day rehydration at 25 °C. The frequency at 1632  $cm^{-1}$  is  $KHCO_3$  specific. Crystal water OH stretch is situated around 3150  $cm^{-1}$ .

a desiccator in air atmosphere for 8 weeks and presence of  $KHCO_3$  was checked using infrared (IR) spectroscopy. No quantitative information could be deduced due to the limited penetration depth of infra red. Fig. 9, spectrum (a) and (b) are literature spectra of anhydrous  $K_2CO_3$  and  $KHCO_3$  [34]. (c) shows an experimental spectrum of  $K_2CO_3 \cdot 1.5H_2O$ . (d) shows the same spectrum after 8 weeks of storage inside a desiccator. The characteristic frequency at 1632  $cm^{-1}$  belongs to  $KHCO_3$ , also present in experimental spectrum (e) of  $KHCO_3$ . Judged from spectra (c) and (d),  $KHCO_3$  forms during storage of  $K_2CO_3$  in air. The  $KHCO_3$  impurity could be removed by heating (as predicted by the phase diagram in Fig. 8 -spectrum (f)) and was not detected after 1 day of in-situ rehydration at lab conditions of 21 °C  $p_{H_2O} \sim 10$  mbar. This indicates that  $CO_2$  adsorption by  $K_2CO_3$  (reaction (15b)) is slow compared to  $H_2O$  adsorption (reaction (15a)).

$K_2CO_3 \cdot 1.5H_2O$  (50–164  $\mu$ m) containing  $KHCO_3$  impurity was used in thermal analysis as a worst case scenario for thermochemical

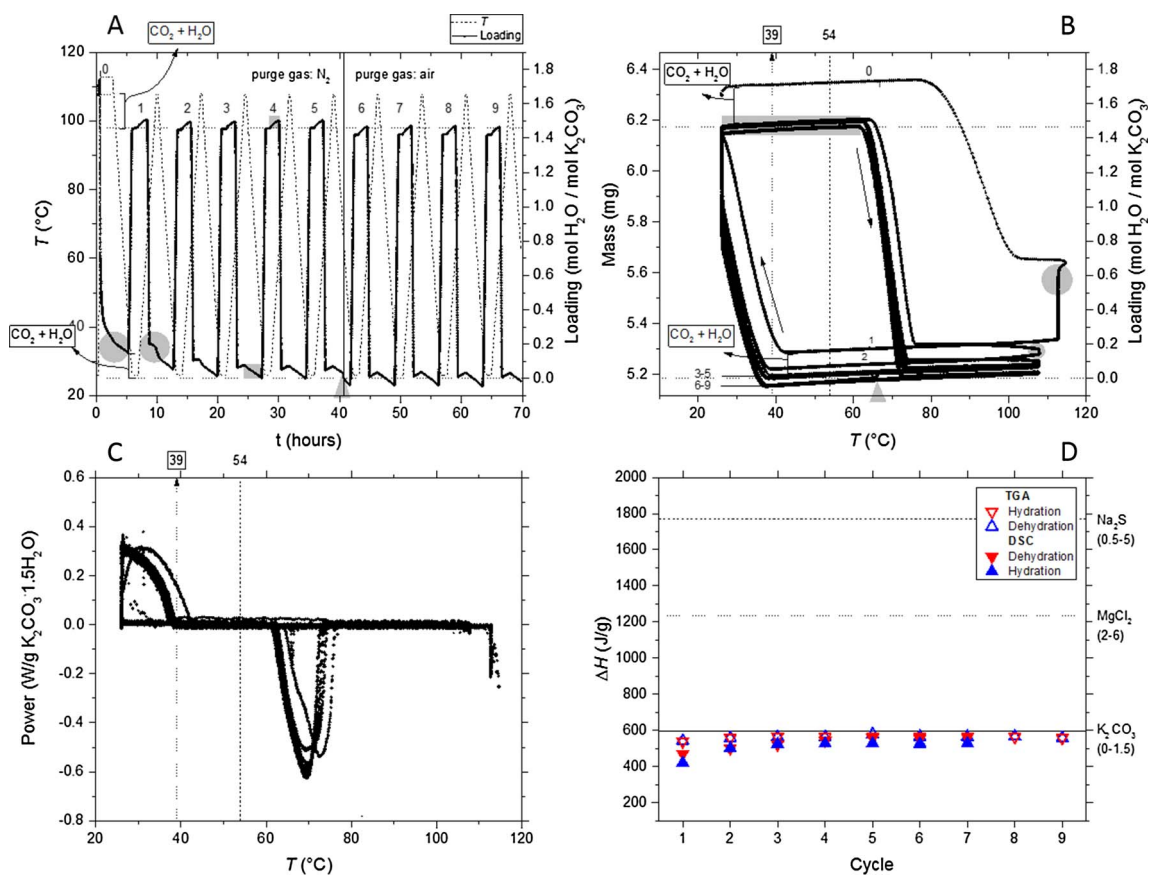


**Fig. 10.** (A) Thermogram of nine consecutive hydrations of  $K_2CO_3$ . Loading (mol  $H_2O/mol K_2CO_3$ ) and sample temperature ( $^{\circ}C$ ) are plotted against time. Temperature range 25–107  $^{\circ}C$ ,  $p_{H_2O} = 7.5$  mbar, heating/cooling rate 0.5 K/min. (B) Mass and loading against sample temperature, (C) power against sample temperature, and (D) the enthalpy of transition in the course of cycles.

application. Results of thermal analysis are summarised in Fig. 10.

Fig. 10a displays the water loading and sample temperature for nine subsequent cycles of hydration. The horizontal dotted lines represent the minimum and maximum loading observed. Inert  $N_2$  was used as purge gas in cycles 1–5 to mimic the non-reactive conditions in a closed system. After 5 cycles, the purge gas was switched to air (0.4 mbar  $CO_2$ ) to mimic the reactive conditions of an open system. Artefacts caused by buoyancy and purge gas change are indicated by the grey rectangles and triangle respectively.

Water uptake occurs reproducibly after 3 cycles of hydration. No difference in hydration behaviour is observed when switching from  $N_2$  to air purge.

$KHCO_3$  presence causes the anomaly in the dehydrations prior to cycle 1 and 2, indicated by the grey circles. TGA-based amount of  $KHCO_3$ -impurity prior to each hydration is calculated in two ways: (1) Using the mass balance based on Eq. (15a) and (2) Using the mass balance based on reactions (15b) and (15c). The mass% impurity prior to each hydration is displayed in Fig. 11. The maximum transition observed in this experiment is 0–1.47 rather than 0–1.5 based on the mass balance in (15a), corresponding to an impurity level of 2%.

Fig. 10b displays the sample mass and loading against temperature. In this view, the onset temperature (dotted arrow) is compared with the thermodynamically expected onset temperature of 54  $^{\circ}C$  at  $p_{H_2O} = 7.5$  mbar (dashed line). Hydration starts at 39  $^{\circ}C$ . Mass changes are calculated to power output and plotted against sample temperature, presented in graph 10c. Hydration of  $K_2CO_3$  produces a peak power of 0.31 W/g at 32  $^{\circ}C$ .

As a final experiment, the multi-cyclic heat in- and output was measured directly using DSC. Conditions favourable for  $KHCO_3$  formation were imposed to test the effect on heat in- and output. Humid

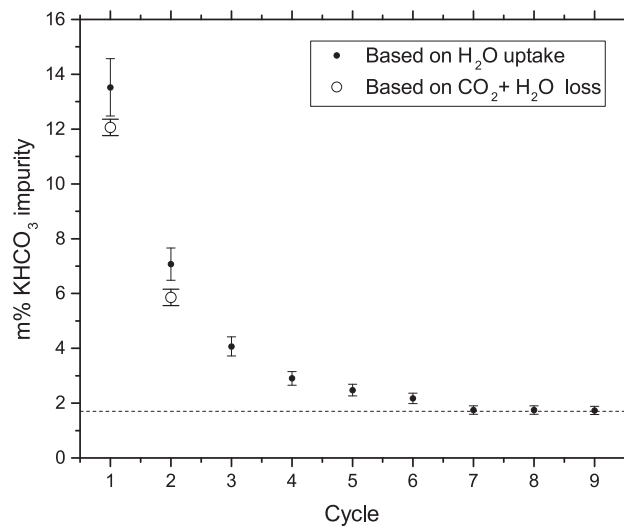


**Fig. 11.** Mass %  $KHCO_3$  impurity prior to each hydration. Calculated based on (1) water uptake. I.e., mass  $K_2CO_3/K_2CO_3 \cdot 1.5H_2O$  expected based on mass change due to water sorption compared to the actual mass in  $K_2CO_3/K_2CO_3 \cdot 1.5H_2O$  state (closed circles). (2) Loss of  $CO_2 + H_2O$  (open circles).

air ( $p_{CO_2} = 0.4$  mbar and  $p_{H_2O} = 18$  mbar) was used as purge gas and temperature range of 25–115 was applied seven times using a heating/cooling rate of 0.75 K/min.

The DSC thermogram is presented in Fig. 12. It is likely that the endothermic signal indicated by the grey circles is  $CO_2$  desorption. Assuming 10 m%  $KHCO_3$ , the estimated reaction enthalpy for reaction

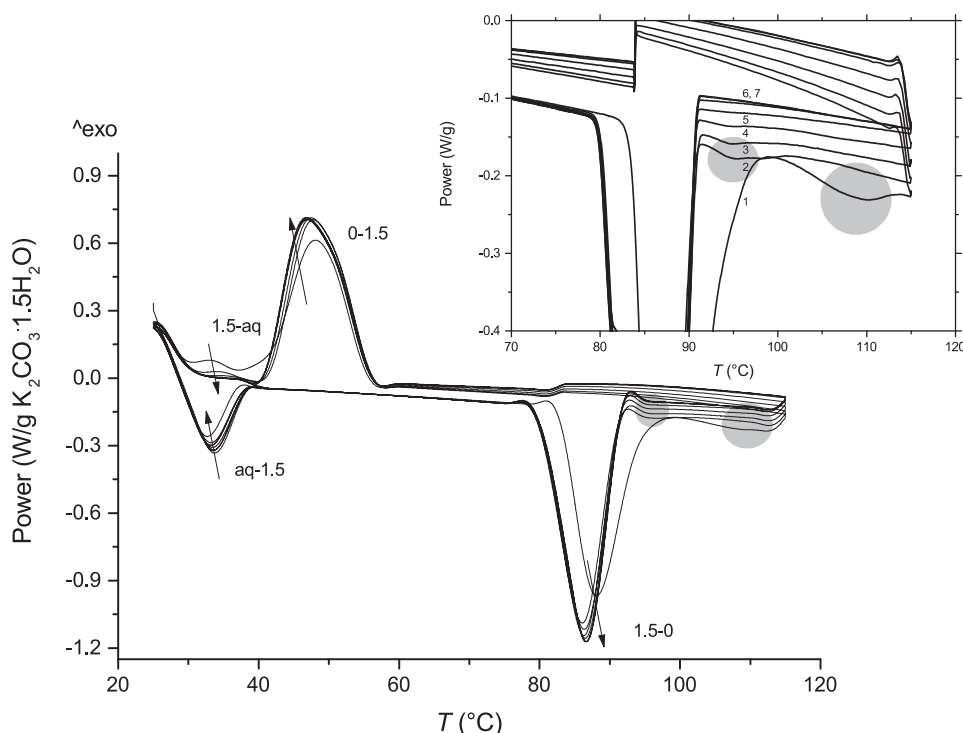


**Fig. 12.** DSC curve of  $K_2CO_3 \cdot 1.5H_2O$ . Heating/cooling rate 0.75 K/min at  $p_{H_2O} = 18$  mbar. In these conditions, deliquescence occurs, promoting the adsorption of  $CO_2 + H_2O$ . Hydration and dehydration is indicated as 0-1.5 and 1.5-0 respectively. Deliquescence and evaporation of deliquescence water is indicated as 1.5-aq and aq-1.5 respectively. Inset: zoom-in on the dehydration. The first dehydration has a slight delay in onset temperature and is followed by a second endothermic signal. The second endothermic signal (indicated by the grey circle) is probably irreversible  $CO_2$  desorption. The energy in- and output is in good agreement with the theoretical enthalpy expected based on the 0-1.5 transition.

(15b) under standard conditions is 164 J/g. The area under the curves indicated by the grey circles is 24 J/g. It is likely that the DSC signal is not acquired in full sensitivity because  $CO_2$  desorption proceeds rather slow. Besides, heat losses caused by the non-optimal contact between salt and Aluminium pan result in underestimation of the calorimetric signal in general for salts.

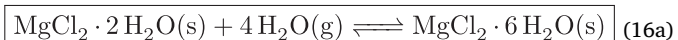
Energy in- and output based on TGA and DSC is presented in Fig. 10d as a function of cycle number. The DSC heat output is in good agreement with the heat output expected based on TGA.

#### 4.2. $MgCl_2$ 2-6 transition

Present literature suggests that  $H_2O$  uptake by  $MgCl_2 \cdot 2H_2O$  to form  $MgCl_2 \cdot 6H_2O$  releases an average binding enthalpy of 58.3–62.8 kJ mol water<sup>-1</sup>, corresponding to a maximum energy density of 1.93 GJ/m<sup>3</sup> [20,5]. The thermochemical reaction is given in reaction (16a) and the corresponding phase diagram is presented in Fig. 13 [20].

HCl formation is a well-known side reaction accompanying the dehydration of magnesium chloride, shown generically in reaction (16b). HCl formation is studied by various authors in different frameworks, without full consensus on the exact temperature of degradation [17,35–40]. Degradation at 110 °C and  $p_{H_2O} = 13$  mbar is reported in recent experimental studies [17].

Phase diagrams of reactions (16a) and (16b) are superimposed in Fig. 14 [11]. The hatched area represents the conditions in which HCl formation occurs. The hatched area is used as an experimental guideline and is partly in agreement with the present literature on HCl formation [35,36].



For constructing the worst case boundary of the hatched area,  $n$  in reaction (16b) was chosen as  $n = 6$  (i.e. chemical degradation of  $MgCl_2 \cdot 6H_2O$ ) and  $p_{HCl}$  was chosen as 0.1 mbar (dotted lines). As a best case scenario,  $n$  was chosen as  $n = 2$  (i.e. chemical degradation of  $MgCl_2 \cdot 2H_2O$ ) and  $p_{HCl} = 1$  mbar (short dotted lines).

Because the degradation reaction involves no other reactive gasses

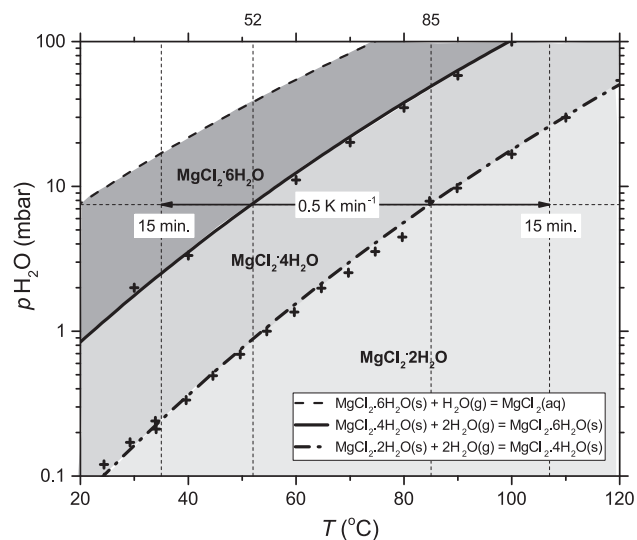


**Fig. 13.** Phase diagram of  $MgCl_2$  [20]. Experimental conditions are indicated by the dotted lines. Temperature range 35–107 °C,  $p_{H_2O} = 7.5$  mbar, heating/cooling rate 0.5 K/min. Area of the lower hydrate phase is featured light grey, higher hydrate phases are shown as darker grey. The thermodynamic onset temperature of the 2-4 and 4-6 transition at  $p_{H_2O} = 7.5$  mbar are indicated at 85 and 52 °C respectively. The deliquescence transition [26] is shown by the dashed line. Crosses represent experimental pressure-temperature values reported in literature.

than  $H_2O$  and intrinsically produced HCl, chemical degradation is expected in an open and closed system. In an open system, complete degradation is possible, because the reactant HCl is removed. In a closed system, building up of HCl would equilibrate material degradation, but might damage the closed reactor by corrosion.

Experimental conditions at which the multi-cyclic energy density was studied are schematically included in the phase diagram in Fig. 13.  $MgCl_2 \cdot 6H_2O$  was dehydrated and rehydrated at  $p_{H_2O} = 7.5$  mbar inside TGA by adapting the sample temperature between 107 °C and 35 °C respectively, with a rate of 0.5 K/min. An isothermal conditioning period of 15 min at 35 °C and 107 °C was used to complete the (de)

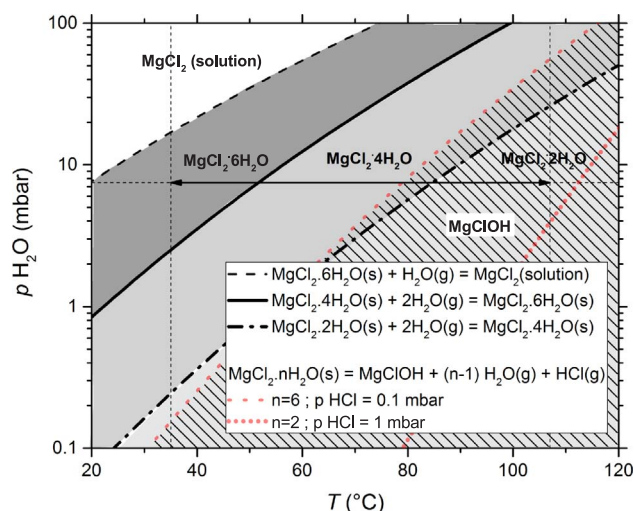


Fig. 14. Phase diagram for reactions (16a) and (16b) at  $p_{\text{HCl}} = 0.1$  mbar,  $n = 6$  (dotted line) and  $p_{\text{HCl}} = 1$  mbar,  $n = 2$  (short dotted lines) [19,11,35]. Experimental working temperatures and pressures are indicated by dotted lines.

hydration before starting the next cycle.

Prior to thermal analysis, a litmus test was performed on closed vials containing  $\text{MgCl}_2 \cdot 6\text{H}_2\text{O}$  stored at 25, 50, 60, 70, 80, 90 and 100 °C. Empty vials with litmus paper were used as blanco. The litmus paper turned red at temperatures of 70 °C and above, which indicates early acid formation in the hexahydrate.

Results of thermal analysis on  $\text{MgCl}_2 \cdot 6\text{H}_2\text{O}$  are summarised in

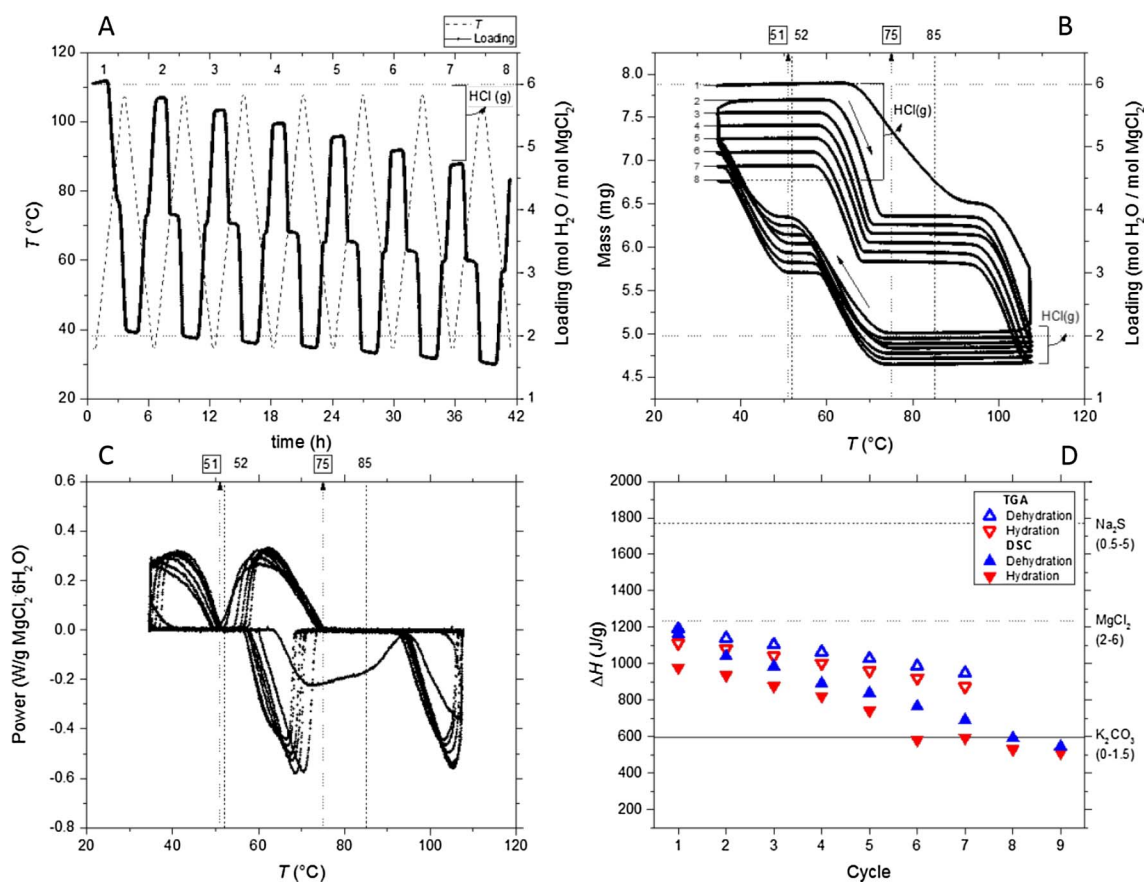


Fig. 15. (A) Thermogram of eight consecutive hydrations of  $\text{MgCl}_2$ . Loading (mol  $\text{H}_2\text{O}$ /mol  $\text{MgCl}_2$ ) and sample temperature (°C) are plotted against time. Temperature range 35–107 °C,  $p_{\text{H}_2\text{O}} = 7.5$  mbar, heating/cooling rate 0.5 K/min. (B) Mass and loading against sample temperature, (C) power against sample temperature, and (D) the enthalpy of transition in the course of cycles.

Fig. 15. Fig. 15a displays the water loading and sample temperature for eight subsequent cycles of hydration. The horizontal dotted lines represent the minimum and maximum loading observed. Water uptake capacity decreases over cycles rapidly. Based on the water uptake, the active  $\text{MgCl}_2 \cdot 6\text{H}_2\text{O}$  fraction is decreasing 3.4% each cycle, meaning that the compound has fully degraded after 30 cycles. In this experiment,  $\text{MgCl}_2 \cdot 6\text{H}_2\text{O}$  was exposed 84 min to temperatures of > 90 °C. This observation is in agreement with recent experimental studies reporting almost complete degradation after 20 cycles at a charging (dehydration) temperature of 110 °C at  $p_{\text{H}_2\text{O}} = 13$  mbar [17].

Fig. 15b displays the sample mass and loading against temperature. In this view, onset temperatures (indicated by the dotted arrows) are compared with the thermodynamically expected onset temperature of 85 °C (2-4 transition) and 52 °C (4-6 transition) at  $p_{\text{H}_2\text{O}} = 7.5$  mbar (indicated by the dashed lines). Hydration starts at 75 °C.

Mass changes are calculated to power output and plotted against sample temperature, presented in Fig. 15c. Hydration of  $\text{MgCl}_2 \cdot 2\text{H}_2\text{O}$  produces a peak power of 0.30 W/g at 63 and 42 °C.

As a final experiment, the multi-cyclic heat in- and output was measured directly using DSC.  $p_{\text{H}_2\text{O}}$  was kept at 7.5 mbar and a temperature range of 35–115 °C was applied twelve times using a heating/cooling rate of 0.1 K/min to acquire the full transition in the imposed temperature range. The DSC thermogram of the first eight cycles is presented in Fig. 16. The power output decreases in the course of cycles.

Energy in- and output as a function of cycle number is presented in Fig. 15d. For a non-degraded sample (i.e. the first dehydration), good correlation between TGA and DSC is observed. In DSC conditions, sample exposure to temperatures > 90 °C was 340 min in each cycle. The active TCM fraction is fully degraded after 15 cycles, based on DSC heat in- and output.

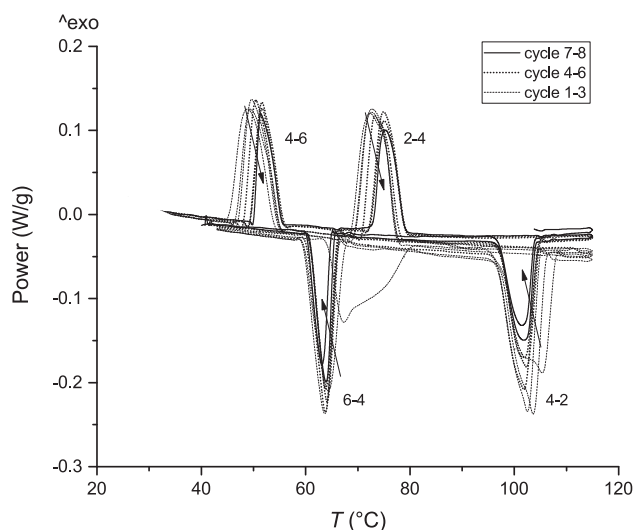


Fig. 16. DSC curve of  $\text{MgCl}_2 \cdot 6\text{H}_2\text{O}$ , 8 cycles of hydration and dehydration at  $p_{\text{H}_2\text{O}} = 7.5$  mbar. Heating/cooling rate 0.1 K/min. The power output in DSC is decreasing over cycles. Transitions are indicated next to the corresponding peak.

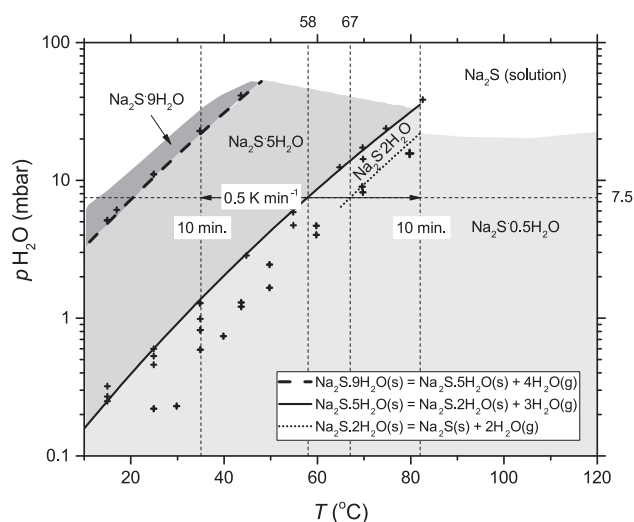


Fig. 17. Phase diagram of  $\text{Na}_2\text{S}$  [18]. Experimental conditions are indicated by the dotted lines. Temperature range 35–80 °C,  $p_{\text{H}_2\text{O}} = 7.5$  mbar, heating/cooling rate 0.5 K/min. Area of the lower hydrate phase is featured light grey, higher hydrate phases are shown as darker grey. The thermodynamic onset temperature of the 2–5 transition at  $p_{\text{H}_2\text{O}} = 7.5$  mbar (observed as 0.5–5 in thermal analysis) is indicated at 58 °C. Crosses represent experimental pressure temperature values reported in literature.

#### 4.3. $\text{Na}_2\text{S} \cdot 0.5\text{H}_2\text{O}$ transition

Present literature suggests that  $\text{H}_2\text{O}$  uptake by  $\text{Na}_2\text{S} \cdot 0.5\text{H}_2\text{O}$  to form  $\text{Na}_2\text{S} \cdot 5\text{H}_2\text{O}$  releases an average binding enthalpy of 65.8 kJ/mol water, corresponding to a maximum energy density of 2.79 GJ/m<sup>3</sup> [5,19]. The high energy density makes  $\text{Na}_2\text{S}$  an interesting compound for heat storage application, studied by various authors [18,41–43]. The thermochemical reaction is given in reaction (17a) and the corresponding phase diagram is presented in Fig. 17 [18]. Although anhydrous  $\text{Na}_2\text{S}$  is reported as crystalline phase [44], no 0–5 transition is reported in literature. Explanations are usually based on the difficulty of removing the last water molecules as the compound is very hygroscopic [18,23]. Another feature of  $\text{Na}_2\text{S}$  is the low melting point.  $\text{Na}_2\text{S} \cdot 5\text{H}_2\text{O}$  has a melting point of 83 °C [18]. Therefore, a maximum temperature of 80 °C was used in multi-cyclic experiments.

After additional literature study on  $\text{Na}_2\text{S}$  reactivity [23,24,45–47], reaction (17b) was found possible as a side reaction to hydration.

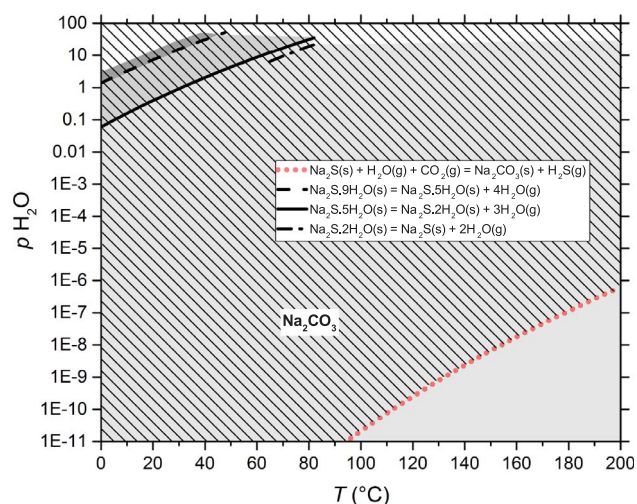


Fig. 18. Phase diagram for reactions (17a) and (17b) at  $p_{\text{H}_2\text{S}} = 0.1$  mbar (100 ppm) and  $p_{\text{CO}_2} = 0.4$  mbar (atmospheric conditions) [19,11]. Based on this,  $\text{Na}_2\text{CO}_3$  is the thermodynamically expected compound if  $\text{Na}_2\text{S} \cdot 5\text{H}_2\text{O}$  is exposed to ambient conditions.

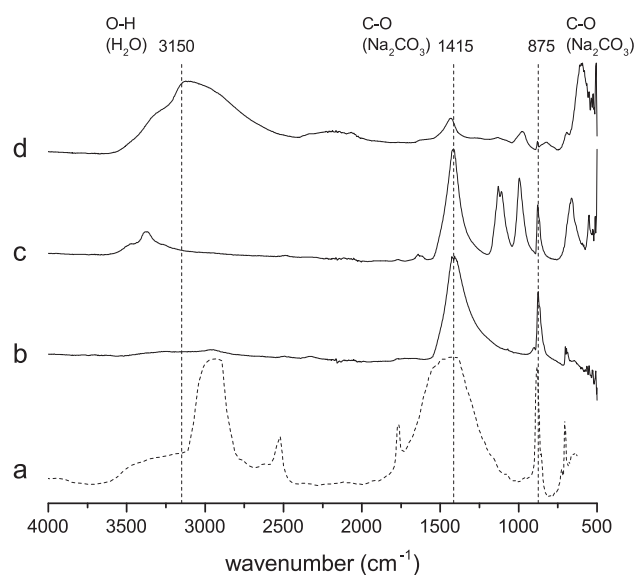
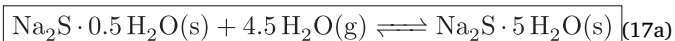


Fig. 19. IR spectra of  $\text{Na}_2\text{S} \cdot 5\text{H}_2\text{O}$  and  $\text{Na}_2\text{CO}_3$ . Experimental and literature [34] spectra are shown in solid and dotted lines respectively. (a)  $\text{Na}_2\text{CO}_3$ , (b)  $\text{Na}_2\text{CO}_3$  pro-analysis Sigma-Aldrich, (c)  $\text{Na}_2\text{S} \cdot 5\text{H}_2\text{O}$  after 1 day in air at 25 °C and (d)  $\text{Na}_2\text{S} \cdot 5\text{H}_2\text{O}$ , recrystallised. The frequency at 1632  $\text{cm}^{-1}$  is  $\text{Na}_2\text{CO}_3$  specific [50,51].

Although this reaction is not mentioned in the present thermochemical studies on  $\text{Na}_2\text{S}$  [18,48,49], it plays an important role in the effective energy density. Phase diagrams of reactions (17a and 17b) are superimposed in Fig. 18 to identify thermodynamic conditions for chemical degradation. The hatched area represents the conditions in which  $\text{Na}_2\text{CO}_3$  formation occurs:  $\text{CO}_2$  adsorption is theoretically expected at all temperatures and water vapour pressures in atmospheric conditions. This makes a multi-cyclic experimental study in open and closed system conditions rather necessary. Open and closed system reactive conditions were mimicked by using air and  $\text{N}_2$  as purge gas respectively.

Experimental conditions are schematically shown in the phase diagram in Fig. 17.  $\text{Na}_2\text{S} \cdot 5\text{H}_2\text{O}$  was dehydrated and rehydrated at  $p_{\text{H}_2\text{O}} = 7.5$  mbar inside TGA by adapting the sample temperature between 80 °C and 35 °C respectively, with a rate of 0.5 K/min. An isothermal conditioning period of 10 min at 35 and 80 °C was used to complete the (de)hydration before starting the next cycle.



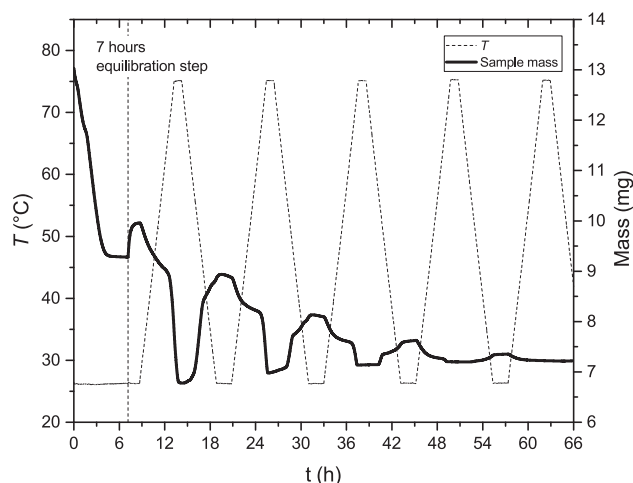
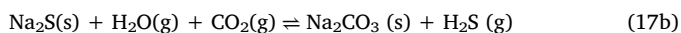


Fig. 20. TGA thermogram of  $\text{Na}_2\text{S}\cdot 5\text{H}_2\text{O}$  in air atmosphere. Equilibrated for 7 h at  $p_{\text{H}_2\text{O}} = 7.5$  mbar and continued hydration/dehydration at  $p_{\text{H}_2\text{O}} = 12$  mbar.



Prior to thermal analysis, IR measurements were performed to detect the presence of  $\text{Na}_2\text{CO}_3$  before and after exposure to air; presented in Fig. 19. Spectrum (a) is a literature spectrum of  $\text{Na}_2\text{CO}_3$  [34]. Spectrum (b) is an experimental spectrum of anhydrous  $\text{Na}_2\text{CO}_3$ , showing the  $\text{CO}_3$  specific frequencies at 1415 and  $875\text{ cm}^{-1}$ . Spectrum (c) belongs to  $\text{Na}_2\text{S}$  stored in a desiccator in ambient for 1 week, showing the  $\text{CO}_3$  specific frequencies. (d) shows the spectrum of fresh

$\text{Na}_2\text{S}\cdot 5\text{H}_2\text{O}$ , a clear water peak is present, besides minor  $\text{CO}_3$  peaks. This is probably because the carbonate is spectrally masked by the presence of adsorbed  $\text{H}_2\text{O}$  [23]. Based on IR, it is concluded that  $\text{Na}_2\text{S}\cdot 5\text{H}_2\text{O}$  is difficult to maintain in pure form, because  $\text{Na}_2\text{CO}_3$  formation starts almost instantly in ambient. IR experiments were not continued further, to protect the IR equipment from corrosive  $\text{H}_2\text{S}$  gas.

The multi-cyclic performance of  $\text{Na}_2\text{S}$  was tested initially in air under working conditions of  $p_{\text{H}_2\text{O}} = 12$  mbar. Fig. 20 shows a TGA thermogram of multi-cyclic hydration in air atmosphere. Full degradation in air atmosphere is visible after 4 cycles of hydration. Heating of the sample in the presence of  $\text{CO}_2$  and  $\text{H}_2\text{O}$  is suggested to speed up reaction (17b) [23].

Next, a fresh sample was cycled using  $\text{N}_2$  as purge gas, applying the temperature pressure profile as shown in Fig. 17. Fig. 21a displays the water loading and sample temperature of nine subsequent cycles of hydration. The horizontal dotted lines represent the minimum and maximum loading observed. A stable hydration performance is observed in inert conditions.

Fig. 21b displays the sample mass and loading against temperature. In this view, onset temperatures (indicated by the dotted arrows) are compared with the thermodynamically expected onset temperature of  $58^\circ\text{C}$  at  $p_{\text{H}_2\text{O}} = 7.5$  mbar (indicated by the dashed line). Hydration starts slightly below  $58^\circ\text{C}$  (at  $61^\circ\text{C}$ ), which is interpreted as the delayed 0–2 transition (expected thermodynamically at  $71^\circ\text{C}$ ) [18]. Hydration of a possible  $\text{Na}_2\text{CO}_3/\text{Na}_2\text{S}$  mix is not expected at  $61^\circ\text{C}$ , because  $\text{Na}_2\text{CO}_3$  hydration occurs at temperatures below  $35^\circ\text{C}$  [19,52].

Mass changes are calculated to power output and plotted against sample temperature, presented in Fig. 21c. Hydration of  $\text{Na}_2\text{S}\cdot 0.5\text{H}_2\text{O}$  produces a peak power of  $0.55\text{ W/g}$  at  $45^\circ\text{C}$ . The heat in- and output, based on TGA and DSC is shown in Fig. 21d.

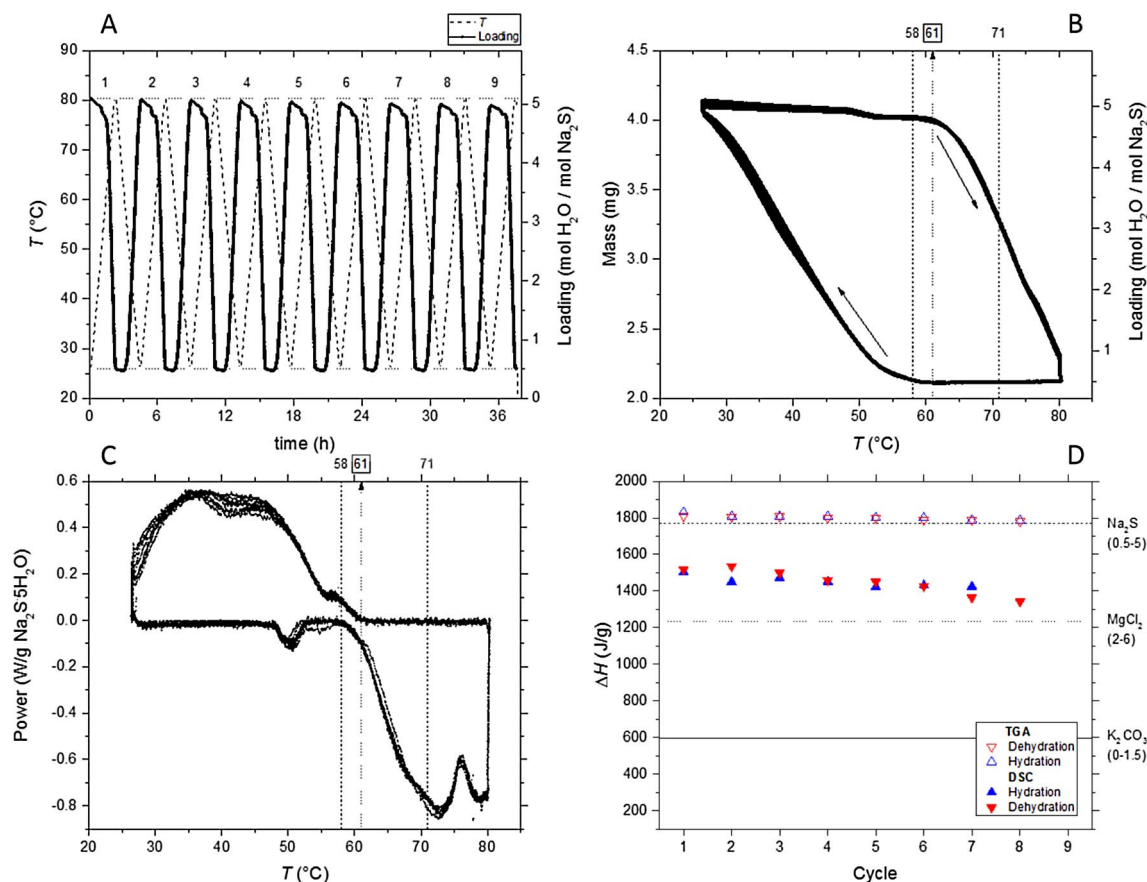


Fig. 21. Thermogram of nine consecutive hydrations of  $\text{Na}_2\text{S}$ . Loading ( $\text{mol H}_2\text{O}/\text{mol Na}_2\text{S}$ ) and sample temperature ( $^\circ\text{C}$ ) are plotted against time. Temperature range  $25\text{--}80^\circ\text{C}$ ,  $p_{\text{H}_2\text{O}} = 7.5$  mbar, heating/cooling rate  $0.5\text{ K}/\text{min}$ . (B): mass and loading against sample temperature, (C): power against sample temperature, and (D): the enthalpy of transition in the course of cycles.

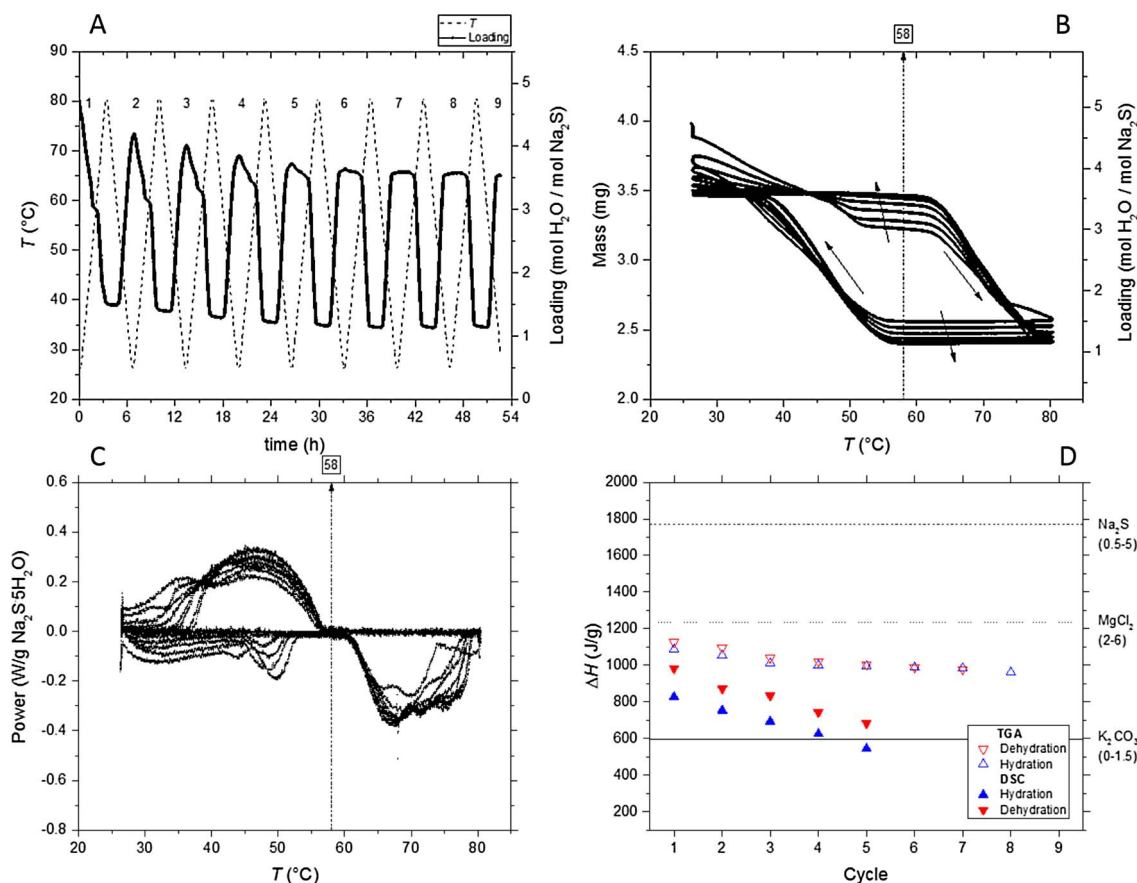


Fig. 22. Thermogram of nine consecutive hydrations of Na<sub>2</sub>S after pre-exposure to air. Loading (mol H<sub>2</sub>O/mol Na<sub>2</sub>S) and sample temperature (°C) are plotted against time. Temperature range 25–80 °C, p<sub>H<sub>2</sub>O</sub> = 7.5 mbar, heating/cooling rate 0.5 K/min. (B): mass and loading against sample temperature, (C): power against sample temperature, and (D): the enthalpy of transition in the course of cycles.

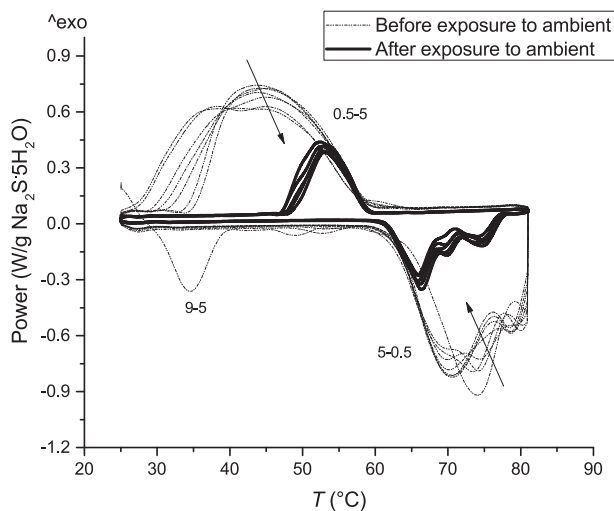


Fig. 23. DSC curve of Na<sub>2</sub>S·5H<sub>2</sub>O, hydration and dehydration at p<sub>H<sub>2</sub>O</sub> = 7.5 mbar. Heating/cooling rate 0.5 K/min. The power output of fresh Na<sub>2</sub>S·5H<sub>2</sub>O is decreasing gradually over cycles, which could be due to minor amounts of CO<sub>2</sub> entering the DSC chamber during sample insertion. Transitions are indicated next to the corresponding peak.

The sensitivity of the cyclic performance of Na<sub>2</sub>S to air exposure was tested by removing the sample from the N<sub>2</sub> atmosphere TGA. The sample was pre-exposed to ambient air for 2 h and the measurement was continued in N<sub>2</sub> atmosphere. Fig. 22a shows the thermogram of Na<sub>2</sub>S after the sample was exposed to ambient air. The chemical

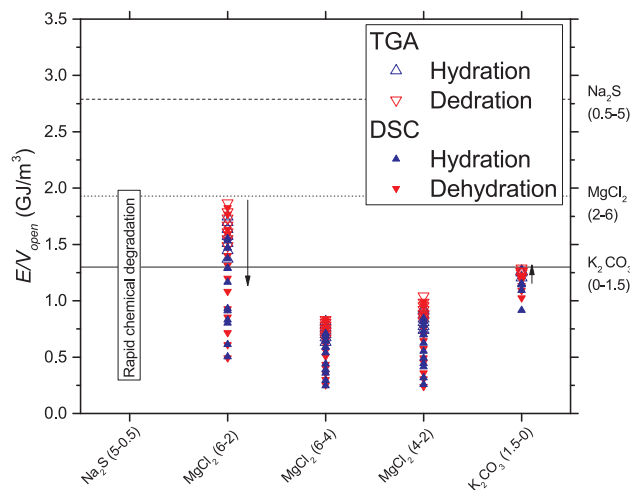
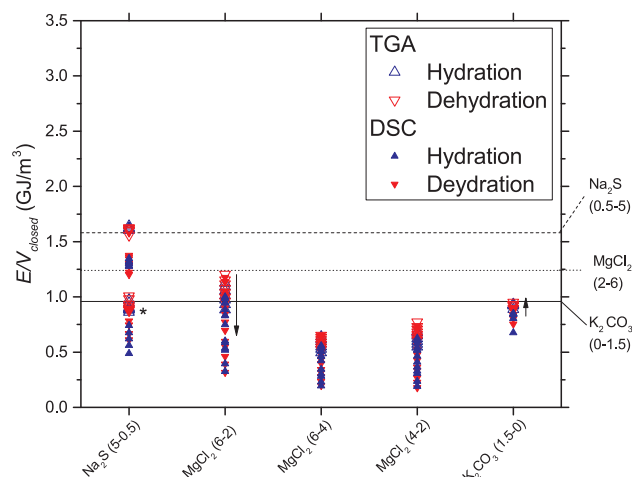


Fig. 24. Experimental energy densities, based on TGA and DSC measurements at p<sub>H<sub>2</sub>O</sub> = 7.5 mbar. Calculated for an open system concept. Theoretical energy densities are indicated with lines. Na<sub>2</sub>S shows no water sorption in air atmosphere, due to rapid degradation to Na<sub>2</sub>CO<sub>3</sub>.

degradation ends in N<sub>2</sub> atmosphere. After 5 cycles, a stable hydration -dehydration pattern is visible, with 55% of the initial water sorption capacity. The inactive part of the material (45%) is Na<sub>2</sub>CO<sub>3</sub>. The sample was probably overhydrated in ambient atmosphere, hence the slight difference over cycles 1–5.

Fig. 22b displays the sample mass and water loading as a function of temperature. Fig. 22c shows the output power, based on mass change



**Fig. 25.** Experimental energy densities, based on TGA and DSC measurements at  $p_{\text{H}_2\text{O}} = 7.5$  mbar. Calculated for an closed system concept. Theoretical energy densities are indicated with lines.  $\text{Na}_2\text{S}$  was measured before and after a pre-exposure of 2 h to air. The measurement after pre-exposure is indicated with (\*).

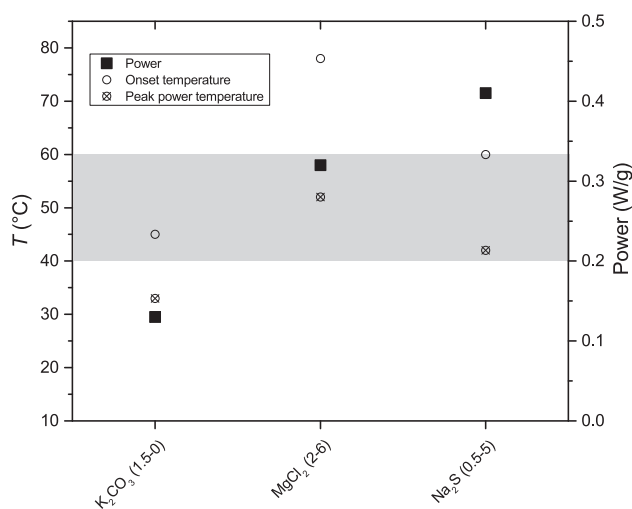


**Fig. 26.** Overview of hydration onset temperature, peak power and peak power temperature at  $p_{\text{H}_2\text{O}} = 12$  mbar. Cooling rate 10 K/min. Sample grains size 0.5–1 mm.

inside TGA. The onset temperature and power output are not significantly affected by the chemical degradation. The heat in- and output, based on TGA and DSC is shown in Fig. 22d, while the DSC measurement is shown in Fig. 23. The heat output after exposure to air is approximately halve of the heat output before exposure (Fig. 21d). This demonstrates that the energy density of  $\text{Na}_2\text{S}$  diminishes rapidly if exposed to atmosphere. The purity of the sample is difficult to control during sample insertion into the thermal analysis equipment, because of the high  $\text{CO}_2$  sensitivity. This causes a mismatch between DSC and TGA heat outputs (solid and open symbols respectively).

#### 4.4. Heat storage performance in view of application

Gravimetric and calorimetric energy densities, calculated for an open and closed system are shown in Figs. 24 and 25, respectively.  $\text{K}_2\text{CO}_3$  has a robust energy density, determined as  $1.28 \text{ GJ/m}^3$  for an open system and  $0.95 \text{ GJ/m}^3$  for a closed system. Given the chemical robustness and the power output of  $\text{K}_2\text{CO}_3$ ,  $1 \text{ m}^3$  of material can be used with a frequency of 12–52 cycles a year (i.e. monthly to weekly), yielding a year basis energy of 15–66 GJ, which can be maintained over at least 20 years.

The material level energy densities of  $\text{MgCl}_2$  and  $\text{Na}_2\text{S}$  in one cycle

**Table 3**

Overview of output powers and temperatures at two testing conditions. Top: Purified material of different grain sizes. Hydration conditions:  $p_{\text{H}_2\text{O}} = 7.5$  mbar (cooling rate 0.5 K/min). Bottom: Materials of 0.5–1 mm grain size. Hydration conditions:  $p_{\text{H}_2\text{O}} = 12$  mbar (cooling rate 10 K/min). In the latter, it was not possible to obtain  $\text{Na}_2\text{S}$  in pure state as grains of 0.5–1 mm. The transition corresponding to the thermodynamic onset temperature is given between brackets.

	$\text{K}_2\text{CO}_3$	$\text{MgCl}_2$	$\text{Na}_2\text{S}$
Transition	0-1.5	2-4-6	0.5-5
<b>7.5 mbar (cooling rate – 0.5 K/min)</b>			
Grain sizes ( $\mu\text{m}$ )	50–164	500–1000	50–164
Thermodynamic onset temperature	53	85 (2-4); 52 (4-6)	58 (0.5 – 5)
Hydration start temperature ( $\pm 0.5$ °C)	42	75; 51	60
Peak power temperature ( $\pm 0.5$ °C)	29	63; 42	45
Peak power ( $\pm 0.01$ W/g)	0.31	0.33; 0.31	0.53
Energy density cycle 1 ( $\text{GJ/m}^3 \pm 0.02$ )	1.21	1.87	2.87
Energy density cycle 8 ( $\text{GJ/m}^3 \pm 0.02$ )	1.28	1.43	2.81
<b>12 mbar (cooling rate – 10 K/min)</b>			
Grain size (mm)	0.5–1	0.5–1	0.5–1
Thermodynamic onset temperature	59	93 (2-4); 61 (4-6)	66 (0.5-5)
Hydration start temperature ( $\pm 0.5$ °C)	45	78	60
Peak power temperature ( $\pm 0.5$ °C)	33	52	42
Peak power ( $\pm 0.01$ W/g)	0.13	0.32	0.41
Energy density cycle 1 ( $\text{GJ/m}^3 \pm 0.02$ )	1.14	1.79	1.44
Energy density cycle 5 ( $\text{GJ/m}^3 \pm 0.02$ )	1.29	1.59	1.37
Stable in closed system?	yes	no	yes
Stable in open system?	yes	no	no
Remark	$\text{KHCO}_3$ impurity is baked out during use	HCl formation	Rapid and complete degradation in air. No inleak air allowed

are higher than the material level energy density of  $\text{K}_2\text{CO}_3$ , matching 1.81 and  $2.81 \text{ GJ/m}^3$  respectively. However, this energy density is not stable over cycles.  $\text{MgCl}_2$  faces thermolysis at thermochemical heat storage conditions, which inactivates the heat storage material completely after a maximum of 30 cycles.  $\text{Na}_2\text{S}$  on the other hand, is air sensitive and can only be used in a closed system, reducing the effective energy density to  $1.64 \text{ GJ/m}^3$  for a pure compound, and down to  $0.95 \text{ GJ/m}^3$  in realistic scenarios where inevitable air-induced degradation is the case. The main challenge for  $\text{Na}_2\text{S}$  is material purity and realisation of a hermetically closed system, which will raise costs of a potential reactor.

Considering output powers and temperatures, multi-cyclic experiments were repeated on 0.5–1 mm sized grains at  $p_{\text{H}_2\text{O}} = 12$  mbar, presented in Fig. 26. Experiments were conducted in air atmosphere, except in the case of  $\text{Na}_2\text{S}$ . Table 3 summarises the results.  $\text{K}_2\text{CO}_3$  has an output power of 0.13 W/g (grain size 500  $\mu\text{m}$ ) to 0.31 W/g (grain size 50  $\mu\text{m}$ ). This power output is low, compared to  $\text{MgCl}_2$  and  $\text{Na}_2\text{S}$ , which provide 0.32 and 0.41 W/g (grain size 500  $\mu\text{m}$ ) respectively. Furthermore,  $\text{K}_2\text{CO}_3$  has a hydration onset temperature of 45 °C, whereas  $\text{Na}_2\text{S}$  and  $\text{MgCl}_2$  have onset temperatures of 60 and 78 °C respectively under the same conditions. Although  $\text{K}_2\text{CO}_3$  has intrinsically a low output power and temperature compared to  $\text{Na}_2\text{S}$  and  $\text{MgCl}_2$ , the power output is sufficient for thermochemical heat storage purpose, with  $283 \text{ kW/m}^3$ . The characteristic discharge temperature of 33–45 °C is too low for generation of hot tap water, but suffices domestic space heating purposes.

## 5. Conclusion

Thermochemical materials  $\text{K}_2\text{CO}_3$ ,  $\text{MgCl}_2$  and  $\text{Na}_2\text{S}$  have been investigated in depth on energy density, power output and chemical

stability, presenting a critical assessment of potential chemical side reactions in an open and closed reactor concept. With  $\text{MgCl}_2$  and  $\text{Na}_2\text{S}$  being thermochemical materials investigated in previous thermal storage research programs, and  $\text{K}_2\text{CO}_3$  being selected among 600 hydrate reactions, performances were evaluated within the frame of a thermochemical battery in the built environment.

$\text{Na}_2\text{S}$  has a superior energy density, output power and temperature ( $2.81 \text{ GJ/m}^3$ , with  $530 \text{ W/kg}$  at a maximum temperature of  $60^\circ\text{C}$ ), but is too air-sensitive for robust application. It is not suitable for use in an open reactor, degrading fully in four cycles. A closed reactor is highly challenging, because of the high demands for vacuum and TCM-production.  $\text{MgCl}_2$  is found not suitable in both open and closed reactor concept, despite the higher energy density, output power and temperature compared to  $\text{K}_2\text{CO}_3$  ( $1.87 \text{ GJ/m}^3$ , with  $330 \text{ W/kg}$  at a maximum temperature of  $75^\circ\text{C}$ ) because of complete degradation of the compound in approximately 30 cycles at temperatures above  $50^\circ\text{C}$ .

The recommended material for further development in thermochemical heat storage application is  $\text{K}_2\text{CO}_3$ . Judged by gravimetric and calorimetric experiments in both operating and worst-case-scenario conditions, it is concluded that  $\text{K}_2\text{CO}_3$  is chemically robust in both an open and closed system. The energy density on material level amounts  $1.28 \text{ GJ/m}^3$  in an open system and  $0.95 \text{ GJ/m}^3$  in a closed system. The power output on material level ranges between  $283$  and  $675 \text{ kW/m}^3$ , depending on the granule size, exceeding the current EU target of  $5 \text{ kW}$  for a single family home. Given the chemical robustness and the power output of  $\text{K}_2\text{CO}_3$ ,  $1 \text{ m}^3$  of material can be used with a frequency of 12–52 cycles a year (i.e. monthly to weekly), yielding a year basis energy of 15–66 GJ, which can be maintained over at least 20 years. The characteristic discharge temperature of  $33$ – $45^\circ\text{C}$  is too low for generation of hot tap water, but suffices domestic space heating purposes.

## Acknowledgements

This project has received funding from the European Union's Horizon 2020 research and innovation programme under grant agreement No. 680450. This work reflects only the author's view. The European Commission is not responsible for any use that may be made of this information.

We thank Dr. A. Anastasopol for supplying recrystallised  $\text{Na}_2\text{S}\cdot 5\text{H}_2\text{O}$  and J. Houben for his help in building the pressure temperature set-up.

## References

- [1] H2020-eu.2.1.5.2. – technologies enabling energy-efficient systems and energy-efficient buildings with a low environmental impact; 2014. < [http://cordis.europa.eu/programme/rcn/664201\\_en.html](http://cordis.europa.eu/programme/rcn/664201_en.html) > .
- [2] Belaid F. Understanding the spectrum of domestic energy consumption: empirical evidence from France. *Energy Policy* 2016;92:220–33.
- [3] Kamp H. Warmtevisie; 2015.
- [4] Lizana J, Chacartegui R, Barrios-Padura A, Valverde JM. Advances in thermal energy storage materials and their applications towards zero energy buildings: a critical review. *Appl Energy* 2017;203:219–39.
- [5] Donkers PAJ, Sögütöglu LC, Huinink HP, Fischer HR, Adan OCG. A review of salt hydrates for seasonal heat storage in domestic applications. *Appl Energy* 2017;199:45–68. <http://dx.doi.org/10.1016/j.apenergy.2017.04.080>.
- [6] N'Tsoukpoe KE, Liu H, Pierrès NL, Luo L. A review on long-term sorption solar energy storage. *Renew Sustain Energy Rev* 2009;13(9):2385–96. <http://dx.doi.org/10.1016/j.rser.2009.05.008>. URL: < <http://www.sciencedirect.com/science/article/pii/S1364032109001129> > .
- [7] Roelands M, Cuypers R, Kruij KD, Oversloot H, de Jong A-J, Duvalois W, et al. Preparation & characterization of sodium sulfide hydrates for application in thermochemical storage systems. *Energy Procedia* 2015;70(0):257–66. <http://dx.doi.org/10.1016/j.egypro.2015.02.122>. URL: < <http://www.sciencedirect.com/science/article/pii/S1876610215002441> > .
- [8] Kaygusuz K. The viability of thermal energy storage. *Energy Sources* 1999;21(8):745–55.
- [9] Mehling H, Cabeza LF. Heat and cold storage with PCM. Springer; 2008.
- [10] Goldstein M. Some physical chemical aspects of heat storage. In: UN conf new sources energy, Rome, vol. III; 1961. p. 411–7.
- [11] Wagman D, Evans W, Parker V, Schumm R, Halow I, Bailey S, et al. The NBS tables of chemical thermodynamic properties. *J Phys Chem Ref Data* 1982;11(2):302. URL: < <http://www.nist.gov/data/PDFfiles/jpcrdS2Vol11.pdf> > .
- [12] Rubitherm phase change materials. < <http://www.rubitherm.eu/en/index.html> > [accessed January 12, 2018].
- [13] Zondag H, Kikkert B, Smeding S, de Boer R, Bakker M. Prototype thermochemical heat storage with open reactor system. *Appl Energy* 2013;109:360–5. <http://dx.doi.org/10.1016/j.apenergy.2013.01.082>. URL: < <http://www.sciencedirect.com/science/article/pii/S0306261913001013> > .
- [14] Vanhoudt D, Claessens B, De Ridder F, Reynders G, Cuypers R, Oversloot H, et al. Energy-hub for residential and commercial districts and transport d3.2 report on a combination of thermal storage techniques and components; 2014.
- [15] Mi X, Liu R, Cui H, Memon SA, Xing F, Lo Y. Energy and economic analysis of building integrated with PCM in different cities of China. *Appl Energy* 2016;175:324–36. <http://dx.doi.org/10.1016/j.apenergy.2016.05.032>. URL: < <http://www.sciencedirect.com/science/article/pii/S0306261916306262> > .
- [16] Cabeza LF, Corberan JM, Fevrier N, Landolina S, Monsberger M, Nowak T, et al. Cross-cutting technology roadmap european technology platform on renewable heating and cooling; 2014.
- [17] Ferchaud C. Experimental study of salt hydrates for thermochemical heat storage [Ph.D. thesis]. Technical University Eindhoven; 2015.
- [18] De Boer R, Haije W, Veldhuis J. Determination of structural, thermodynamic and phase properties in the  $\text{Na}_2\text{S}\text{-H}_2\text{O}$  system for application in a chemical heat pump. *Thermochim Acta* 2002;395(1):3–19.
- [19] Washburn E. International critical tables of numerical data, physics, chemistry and technology. 1st Electronic ed. Knovel; 2003. URL: < <http://app.knovel.com/hotlink/toc/id:kpICTNDPC4/international-critical/international-critical> > .
- [20] Carling R. Dissociation pressures enthalpies of reaction in  $\text{MgCl}_2\text{-H}_2\text{O}$  and  $\text{CaCl}_2\text{-nNH}_3$ . *J Chem Thermodyn* 1981;13:503–12.
- [21] Glasser L, Jenkins HDB. The thermodynamic solvate difference rule: solvation parameters and their use in interpretation of the role of bound solvent in condensed-phase solvates. *Inorg Chem* 2007;46(23):9768–78.
- [22] Atkins PW, De Paula J. Atkins' physical chemistry. Oxford Univ. Press; 2010.
- [23] Nash DB. Infrared reflectance spectra of  $\text{Na}_2\text{S}$  with contaminant  $\text{Na}_2\text{CO}_3$ : effects of adsorbed  $\text{H}_2\text{O}$  and  $\text{CO}_2$  and relation to studies of io. *Icarus* 1988;74(2):365–8.
- [24] Güler H, Kurtuluş F, Kadan İ, Morkan A, Akın S. The synthesis of sodium sulfide pentahydrate,  $\text{Na}_2\text{S}\cdot 5\text{H}_2\text{O}$ , through a solid-gas reaction of sulfidizing gas mixture with sodium carbonate,  $\text{Na}_2\text{CO}_3$ . *Phosphorus Sulfur Silicon* 2006;181(6):1371–9.
- [25] Zhao C, Chen X, Zhao C, Liu Y. Carbonation and hydration characteristics of dry potassium-based sorbents for  $\text{CO}_2$  capture. *Energy Fuel* 2009;19:1766–9.
- [26] Greenspan L. Humidity fixed points of binary saturated aqueous solutions. *J Res Natl Bureau Stand* 1977;81(1):89–96.
- [27] Gabbott P. Principles and applications of thermal analysis. John Wiley & Sons; 2008.
- [28] Sarge S, Hemminger W, Gmelin E, Höhne G, Cammenga H, Eysel W. Metrologically based procedures for the temperature, heat and heat flow rate calibration of DSC. *J Therm Anal* 1997;49(2):1125–34.
- [29] Gmelin E, Sarge S. Temperature, heat and heat flow rate calibration of differential scanning calorimeters. *Thermochim Acta* 2000;347(1):9–13.
- [30] Luo H, Chioyama H, Thu S, Ohba T, Kanoh H. Kinetics and structural changes in  $\text{CO}_2$  capture of  $\text{K}_2\text{CO}_3$  under a moist condition 4478(1). <http://dx.doi.org/10.1021/acs.energyfuels.5b00578>.
- [31] Guo Y, Zhao C, Li C. Thermogravimetric analysis of carbonation behaviors of several potassium-based sorbents in low concentration  $\text{CO}_2$ . *J Therm Anal Calorim* 2015:441–51. <http://dx.doi.org/10.1007/s10973-014-4207-3>.
- [32] Olk C. Bachelor thesis study of the regeneration of  $\text{K}_2\text{CO}_3\cdot 1.5\text{H}_2\text{O}$  from  $\text{KHCO}_3$  via a temperature and water vapour pressure swing; 2015.
- [33] Lehman RL, Gentry JS, Glumac NG. Thermal stability of potassium carbonate near its melting point. *Thermochimica Acta* 1998;316:1–9.
- [34] Coblenz Society I. Evaluated infrared reference spectra in NIST chemistry WebBook, NIST standard reference database number 69. In: Linstrom PJ, Mallard WG, editors. Gaithersburg MD, 20899: National Institute of Standards and Technology; 2017. <http://dx.doi.org/10.18434/T4D303>.
- [35] Kipouros GJ, Sadoway DR. A thermochemical analysis of the production of anhydrous  $\text{MgCl}_2$ . *J Light Met* 2001;1(2):111–7.
- [36] Pathak AD, Nedea S, Zondag H, Rindt C, Smeulders D. A DFT-based comparative equilibrium study of thermal dehydration and hydrolysis of  $\text{CaCl}_2$  hydrates and  $\text{MgCl}_2$  hydrates for seasonal heat storage. *Phys Chem Chem Phys* 2016;18:10059–69. <http://dx.doi.org/10.1039/C6CP00926C>.
- [37] Rubino A. Seasonal sorption heat storage—research on thermochemical materials and storage performance. In: Proceedings of heat powered cycles conference; 2012.
- [38] Smeets B, Iype E, Nedea SV, Zondag HA, Rindt CC, Smeets B, et al. A DFT based equilibrium study on the hydrolysis and the dehydration reactions of  $\text{MgCl}_2$  hydrates 2013; 124312. <http://dx.doi.org/10.1063/1.4822001>.
- [39] Galwey AK, Laverty GM. The thermal decomposition of magnesium chloride dihydrate. *Thermochim Acta* 1989;138(1):115–27.
- [40] Kashani-Nejad S, Harris R.  $\text{MgOHCl}$  thermal decomposition kinetics. *Metall Mater Trans B* 2005;36(1):153–7.
- [41] Finck C, Henquet E, van Soest C, Oversloot H, de Jong A-J, Cuypers R, et al. Experimental results of a  $3 \text{ kWh}$  thermochemical heat storage module for space heating application. *Energy Procedia* 2014;48:320–6.
- [42] Bales C, Gantenbein P, Hauer A, Henning H-M, Jaenig D, Kerskes H, et al. Thermal properties of materials for thermo-chemical storage of solar heat. A Report of IEA Solar Heating and Cooling programme-Task 32.
- [43] Solé A, Fontanet X, Barreneche C, Fernández AI, Martorell I, Cabeza LF. Requirements to consider when choosing a thermochemical material for solar energy storage. *Sol Energy* 2013;97:398–404.
- [44] Kızılyallı M, Bilgin M. Solid-state synthesis and x-ray diffraction studies of  $\text{Na}_2\text{S}$ . *J Solid State Chem* 1990;85(2):283–92.

- [45] Tran H, Vakkilainen EK. The kraft chemical recovery process. < <http://www.tappi.org/content/events/08kros/manuscripts/1-1.pdf> > [accessed 9 January 2017 (date unknown)].
- [46] Lindedahl KL. Chemical reactions in Kraft pulping; 2008. < <http://www.h2obykl.com/images/Reactions%20in%20Kraft%20Pulping.pdf> > [accessed 9 January 2017].
- [47] Biermann CJ. Handbook of pulping and papermaking. Academic Press; 1996. URL: < <http://www.sciencedirect.com/science/article/pii/B978012097362050008X> > .
- [48] Andersson JANY, Pablo JDE. Kinetics of the rehydration of sodium sulphide dehydrated in situ. Under Form Pentahydrate 1985;91:223–34.
- [49] Andersson JY, Azoulay M. Mechanisms and kinetics of the thermal decomposition of sodium sulphide pentahydrate under controlled water vapour pressure. J Chem Soc Dalton Trans 1986(3):469–75.
- [50] Huang C, Kerr PF. Infrared study of the carbonate minerals. Am Mineral 1960;45(3–4):311–24.
- [51] Miller FA, Wilkins CH. Infrared spectra and characteristic frequencies of inorganic ions. Anal Chem 1952;24(8):1253–94.
- [52] Glasser L. Thermodynamics of inorganic hydration and of humidity control, with an extensive database of salt hydrate pairs. J Chem Eng Data 2014;59(2):526–30.